Multiphase transformation and mechanical analysis of polycrystalline Cu_xLi_ySn nanoparticle during lithiation via phase diagram-guided phase-field approach

Qi Huang [a,*], Simon Daubner [b,c], Daniel Schneider [b,c,*], Xiaoyu Zheng [a], Shuhong Liu [a], Yong Du [a,*], Britta Nestler [b,c]

[a] State Key Lab of Powder Metallurgy, Central South University, 410083, Changsha, China
[b] Institute for Applied Materials (IAM-MMS), Karlsruhe Institute of Technology, Strasse am Forum 7, 76131, Karlsruhe, Germany
[c] Institute of Digital Materials Science (IDM), Karlsruhe University of Applied Science, Moltkestr. 30, 76133, Karlsruhe, Germany

Keywords:
Phase-field model
Sn-based anode
Polycrystalline nanoparticle
Multiphase transformation
Mechanical analysis

A B S T R A C T

The fabrication of tin (Sn)-based materials with exceptional electrochemical and mechanical properties requires a thorough understanding of the multiphase evolution that occurs during lithiation. However, predicting the microstructural changes during this process using analytical models is challenging due to the intricate interactions among electrode materials, cell operating parameters, complex geometries, and polycrystalline structures. To tackle this challenge, we propose the application of the phase-field method in a grand-potential formulation, that is combined with the smooth boundary method to apply constant-current (de-)lithiation boundary conditions. This approach effectively describes the migration of lithium and the multiphase transitions in polycrystalline electrodes with arbitrary geometries. To investigate nanoparticles with hundreds of grains in two/three dimensions efficiently, we have incorporated this model into the self-developed open-source phase-field solver package MInDes in a highly optimized manner. Further, comparing the output voltage of the simulated lithiation process of Li_xSn nanoparticles in three dimensions demonstrates an excellent correlation with experimental results. Based on this, we analyze the mechanical performance of polycrystalline nanoparticles with varying amounts of copper doping and evaluate the maximal von Mises stress during lithiation to predict the onset of crack formation.

1. Introduction

Sn and Sn-based alloys have emerged as highly promising anode materials for future lithium-ion batteries, primarily due to their impressive theoretical capacity of 994 mAh/g [1–3]. However, like Si [4] and Ge [5] anodes, the main challenge associated with Sn anodes lies in their significant volume expansion during the lithiation process [6]. This expansion induces the accumulation of strain [7], plastic yielding [8,9] and crack formation [10–13] within the electrode. Consequently, these phenomena have a direct impact on the output voltage [14], capacity [15,16], lithium migration rate [17,18] and so on.

In general, researchers aim to enhance the mechanical properties of Sn-based anodes through two main approaches. The first approach involves chemical modification, specifically the formation of an SnM alloy by adding another metal element M to Sn. This alloy formation reduces the precipitation of LiSn phase during lithiation and consequently mitigates the expansion rate of the anode. The second approach is a physical modification, which includes anode nanosizing [19], surface coating [20], and morphology design [21]. In 1999, Winter [2] suggested that alloying could decrease the volume expansion rate and improve the cycling performance of Sn anode materials. Subsequent studies involved the preparation of various binary and ternary Sn-M alloys to investigate their electrochemical properties, for instance, Sn–Cu [22–26], Sn–Fe [23,27], Sn–Mn [28], Sn–Sb [29,30], Sn–Ag–Sb [31], Sn–Co [23,32–34], and Sn–Ni [35,36] were investigated. In the case of the Sn–Cu system, the inert element Cu precipitates as a pure Cu phase during lithiation, serving as a buffer phase that reduces volume changes and lessens volume-induced strain energy [20,37,38]. The primary concept behind this method is to alter the phase transition path of pure Sn during the lithiation process, thereby minimizing the likelihood of substantial volume expansion.

In recent decades, phase-field method has emerged as a powerful tool for studying the microstructure evolution under the influence

* Corresponding authors.
E-mail addresses: hq5088028@csu.edu.cn (Q. Huang), daniel.schneider@kit.edu (D. Schneider), yong-du@csu.edu.cn (Y. Du).

of various physical phenomena [39–41]. Many previous investigations [42–48] of lithium-rich and lithium-poor two-phase systems assumed a single crystal for the half-cell electrode, and distinguished the two phases based on the concentration difference. Recent works employ the more general concept of the multiphase-field method for polycrystalline [49] and multi-phase battery materials [50]. In previous work [51], we modeled a single-crystal Sn nanoparticle and simulated its multiphase transformation during charge/discharge cycling. Based on this, it is more challenging and meaningful to further investigate the multiphase transformation inside a polycrystalline Cu_xLi_ySn nanoparticle. Moreover, credible phase diagrams and thermodynamic property data are pre-requisites for designing advanced materials through thermodynamic modeling and simulation [52–56]. If the equilibrium states are well-defined and thermodynamic quantities are known, the phase-field method can successfully model the kinetics of (dis-)charge and non-equilibrium phase formation in electrode materials during electrochemical cycling.

Based on previously developed models, we employ the smoothed boundary method [57] within the grand-potential formulation [58] and the constant-current (de-)lithiation method [49] to simulate the lithium migration on the surface and in the bulk of electrode particles with arbitrary geometries. To describe phase transitions within polycrystalline nanoparticles, pair-wise multiphase equations [59] are utilized and a clear differentiation between grains and phases is made during modeling and simulation to ensure that phase transitions occur only within each single grain during lithiation. Our mechanical analysis process employs a two-step return algorithm to solve the elastoplastic equations within the nanoparticle. For the elastic and structurally inhomogeneous system, the phase-field microelasticity theory [60] is employed to predict the elastic strain and then the plastic yield equation [61] is considered to solve the plastic strain. The aforementioned equations are implemented in our self-developed open-source parallel program package, MInDes (**M**icrostructure **In**telligent **Des**ign). We have further optimized the modeling and simulation processes for polycrystalline nanoparticle systems to accelerate simulations and reduce memory consumption. Using these combined approaches, the accuracy of simulations is tested for a polycrystalline Sn nanoparticle in three dimensions (3D) and the enhancement of the mechanical properties is discussed for polycrystalline Cu_xLi_ySn nanoparticles in two dimensions (2D).

2. Methodology

2.1. The governing equations

For the description of the phase transition and mass transport during lithiation of the electrode particle, several field variables are employed. In order to differentiate the various regions in a heterogeneous domain, the volume fractions $\phi^\alpha \in [0,1]$, $\forall \alpha = 1,\dots,N$ are introduced to describe different regions. Some regions are liquid ϕ^l and others solid ϕ^s. All these regions can be arranged in the tuple $\boldsymbol{\phi} = \{\phi^s, \phi^l\} = \{\phi^1, \phi^2, \dots, \phi^N\}$. Since the solid and liquid regions contain different substances and the focus of this work is on the solid phase transitions, diffusion potentials for each components in solid regions $\widetilde{\boldsymbol{\mu}}^s = \{\widetilde{\mu}_1^s, \widetilde{\mu}_2^s, \dots, \widetilde{\mu}_{K-1}^s\}$ are introduced here.

2.1.1. Mass transport equation

First, the component i in solid phases x_i^s is defined as $\phi^s x_i^s = \sum_{\alpha\in s} \phi^\alpha x_i^\alpha$, where volume fraction of solid phases can be calculated by formula $\phi^s = \sum_{\alpha\in s}\phi^\alpha$. Assuming that there is no phase transition between the liquid phase (electrolyte) and solid phases (electrode), i.e. $\partial_t \phi^s = 0$, the following relation can be easily derived

$$\phi^s \frac{\partial x_i^s}{\partial t} = \sum_{\alpha\in s}\phi^\alpha \sum_{k=1}^{K-1} \frac{\partial x_i^\alpha}{\partial \widetilde{\mu}_k^s}\frac{\partial \widetilde{\mu}_k^s}{\partial t} + \sum_{\alpha\in s}\frac{\partial \phi^\alpha}{\partial t} x_i^\alpha. \tag{1}$$

For the purpose of characterizing the mass transport process in solid phases (e.g. effective region is defined as $\phi^s > 0.9$), the smoothed boundary method [57] is introduced

$$\begin{aligned}\phi^s \frac{\partial x_i^s}{\partial t} &= -\phi^s \nabla\cdot \boldsymbol{J_i^s} + \phi^s R_i^s \\ &= -\nabla\cdot\left(\phi^s \boldsymbol{J_i^s}\right) + \nabla\phi^s\cdot \boldsymbol{J_i^s} + \phi^s R_i^s,\end{aligned} \tag{2}$$

where $\boldsymbol{J_i^s}$ is the flux in solid phases and R_i^s the reaction in solid phases. From Eqs. (1) and (2), when condition $\left(\partial x_i^\alpha/\partial\widetilde{\mu}_k^s\right)_{i\neq k} = 0$ is satisfied, the grand-potential equation [58] applicable to an arbitrary-geometry region can be derived

$$\begin{aligned}\frac{\partial \widetilde{\mu}_i^s}{\partial t} = &\left[\sum_{\alpha\in s}\phi^\alpha \frac{\partial x_i^\alpha}{\partial \widetilde{\mu}_j^s}\right]_{ij}^{-1} \\ &\times\left\{\nabla\cdot\sum_{j=1}^{K-1}\widetilde{M}_{ij}(\phi^s)\nabla\widetilde{\mu}_j^s + \nabla\phi^s\cdot\boldsymbol{J_i^s} + \phi^s R_i^s - \sum_{\alpha\in s} x_i^\alpha\frac{\partial\phi^\alpha}{\partial t}\right\},\end{aligned} \tag{3}$$

where the chemical mobility is a function of the phase-dependent diffusivities $\widetilde{M}_{ij}(\phi^s) = \sum_{\alpha\in s}\phi^\alpha D_{ij}^\alpha\left(\partial x_i^\alpha/\partial\widetilde{\mu}_j^s\right)$. The interfacial flux $\nabla\phi^s\cdot\boldsymbol{J_i^s}$ is given by the electrochemical surface reaction which is expressed by the classical Butler–Volmer equation [62]

$$\nabla\phi^s\cdot\boldsymbol{J_i^s} = |\nabla\phi^s|\frac{j_0(x)}{\mathscr{F}}\left\{exp\left(a\frac{e\eta}{k_BT}\right) - exp\left[(a-1)\frac{e\eta}{k_BT}\right]\right\}, \tag{4}$$

where the exchange current density $j_0(x)$ can be computed by formula $j_0 = k_0\sqrt{x(1-x)}$, $\mathscr{F}$ the Faraday's constant, and a a parameter that takes 0.5 when assuming symmetry of the reaction. The driving force for the electrode reaction is given by the jump of electrochemical potentials between the interface of electrode and electrolyte. Assuming that the reaction on the surface of reference cathode and the mass transport in electrolyte are fast [49], the computation of the overpotential can be reduced to the following equation

$$\eta = \frac{\widetilde{\mu}_{\mathrm{Li}}^{ref} - \widetilde{\mu}_{\mathrm{Li}}^s}{RT} = \left(V_{cell}^\theta - V_{app}\right) - \frac{k_BT}{e}\widetilde{\mu}_{\mathrm{Li}}^s, \tag{5}$$

where $\widetilde{\mu}_{\mathrm{Li}}$ is the diffusion potential of lithium, V_{cell}^θ a reference voltage, and V_{app} the applied cell voltage. We apply a constant current boundary condition following the procedure in [49]. In the context of the smooth boundary method, the total influx is given by a volume integral over the diffuse particle boundary

$$I = c_{max}C\text{-}rate\int_V \phi^s dr^3 \overset{\text{def}}{=} \int_V\left(\nabla\phi^s\cdot\boldsymbol{J_i^s}\right)dr^3. \tag{6}$$

By inserting Eqs. (4) and (5) into Eq. (6), the applied voltage V_{app} can be calculated in every timestep for a given total flux I. V_{app} is then re-inserted into Eqs. (4) and (5) to compute the local lithium flux.

2.1.2. Phase transformation equation

In order to investigate polycrystalline electrodes, the free energy functional of the whole system is employed in the Ginzburg–Landau form [51]

$$\begin{aligned}F\left(\boldsymbol{\phi},\nabla\boldsymbol{\phi},\varphi,\widetilde{\boldsymbol{\mu}}^s,\boldsymbol{\epsilon_{el}},\bar{\epsilon}_{pl}\right) &= F_{int}\left(\boldsymbol{\phi},\nabla\boldsymbol{\phi}\right) + F_{bulk}\left(\boldsymbol{\phi},\varphi,\widetilde{\boldsymbol{\mu}}^s,\boldsymbol{\epsilon_{el}},\bar{\epsilon}_{pl}\right) \\ &= \int_V\left(f_{int} + f_{chem} + f_{elec} + f_{mech}\right)dr^3.\end{aligned} \tag{7}$$

The diffuse interface is determined by the interfacial energy density [63]

$$f_{int}\left(\boldsymbol{\phi},\nabla\boldsymbol{\phi}\right) = \sum_{\alpha,\beta>\alpha}\gamma^{\alpha\beta}\left(\frac{16}{\varepsilon\pi^2}\phi^\alpha\phi^\beta - \varepsilon\nabla\phi^\alpha\nabla\phi^\beta\right) \tag{8}$$

with the interfacial energy $\gamma^{\alpha\beta}$ between two phases α and β, and the interface width ε, which prevents the non-physical formation of third phase in binary interfaces. This is important to avoid spurious existence of the liquid phase at grain boundaries in the solid particle which would impair the correct definition of electrochemical surface reactions.

The chemical energy density is defined as the linear interpolation of phase-dependent chemical energies f_{chem}^{α} with the volume fraction ϕ^{α}

$$f_{chem}\left(\boldsymbol{\phi},\widetilde{\boldsymbol{\mu}}^{\boldsymbol{s}}\right)=\sum_{\alpha\in s}\phi^{\alpha}f_{chem}^{\alpha}\left(x_i^{\alpha}\left(\widetilde{\boldsymbol{\mu}}^{\boldsymbol{s}},T\right),T\right). \tag{9}$$

The phase concentration $x_i^{\alpha}\left(\widetilde{\boldsymbol{\mu}}^{\boldsymbol{s}},T\right)$ needs to be calculated from the diffusion potential $\widetilde{\boldsymbol{\mu}}^{\boldsymbol{s}}$, which requires that the diffusion potential functions satisfy the invertibility criterion $\widetilde{\mu}_i^s\left(\boldsymbol{x}^{\boldsymbol{\alpha}},T\right)=\partial f_{chem}^{\alpha}\left(x_i^{\alpha},T\right)/\partial x_i^{\alpha}$.

The electrostatic energy density f_{elec} including electrostatic potential φ is formulated as

$$f_{elec}\left(\boldsymbol{\phi},\varphi,\widetilde{\boldsymbol{\mu}}^{\boldsymbol{s}}\right)=\mathscr{F}\left(V_m\right)^{-1}\varphi\sum_{\alpha\in s}\phi^{\alpha}\sum_i z_i^{\alpha}x_i^{\alpha}\left(\widetilde{\boldsymbol{\mu}}^{\boldsymbol{s}},T\right), \tag{10}$$

where V_m is molar volume, and z_i^{α} the valence of component i in α phase (equiv/mol or charge units per ion).

Assuming that the phase-dependent diffusion potentials are equal to each other at solid–solid interfaces [58], the following equation holds for lithium and likewise for copper

$$\frac{\partial f_{bulk}^{\alpha}}{\partial x_i^{\alpha}}=\frac{\partial f_{bulk}^{\beta}}{\partial x_i^{\beta}}=\cdots=\widetilde{\mu}_i^s. \tag{11}$$

The concentrations of the components within the solid phases fulfill the relation $\phi^s x_i^s=\sum_{\alpha\in s}\phi^{\alpha}x_i^{\alpha}$. According to the law of mass conservation, the following formula can be derived $\sum_{\beta\in s}\phi^{\beta}\partial x_i^{\beta}/\partial\phi^{\alpha}=-x_i^{\alpha}$ [64]. Then, the derivative of the bulk energy with respect to volume fraction ϕ^{α} yields

$$\begin{aligned}\frac{\partial f_{bulk}}{\partial\phi^{\alpha}}&=f_{bulk}^{\alpha}+\sum_{i=1}^{K-1}\left[\sum_{\beta\in s}\frac{\partial f_{bulk}^{\beta}}{\partial x_i^{\beta}}\frac{\partial x_i^{\beta}}{\partial\phi^{\alpha}}\phi^{\beta}\right]\\&=f_{bulk}^{\alpha}+\sum_{i=1}^{K-1}\widetilde{\mu}_i^s\left[\sum_{\beta\in s}\frac{\partial x_i^{\beta}}{\partial\phi^{\alpha}}\phi^{\beta}\right]\\&=f_{bulk}^{\alpha}-\sum_{i=1}^{K-1}\widetilde{\mu}_i^s x_i^{\alpha}.\end{aligned} \tag{12}$$

The phase evolution is governed by the sum of pairwise interactions [59]

$$\frac{\partial\phi^{\alpha}}{\partial t}=\frac{1}{\widetilde{N}\epsilon}\sum_{\beta\neq\alpha}^{\widetilde{N}}\widetilde{L}^{\alpha\beta}\left[\left(\frac{\delta}{\delta\phi^{\beta}}-\frac{\delta}{\delta\phi^{\alpha}}\right)F_{int}+\frac{8}{\pi}\sqrt{\phi^{\alpha}\phi^{\beta}}\Delta^{\alpha\beta}\right]+\frac{\partial\zeta}{\partial\phi^{\alpha}}, \tag{13}$$

where the abbreviation $\Delta^{\alpha\beta}=\left(\partial/\partial\phi^{\beta}-\partial/\partial\phi^{\alpha}\right)F_{bulk}$ is used, $\widetilde{N}$ the number of locally active phases, $\widetilde{L}^{\alpha\beta}$ the mobility of α-β dual interface, and thermal fluctuations ζ are generated at interface to enable heterogeneous nucleation [65], which is discussed in Appendix A.

2.1.3. Mechanical analysis equations

For the analysis of the mechanical property of polycrystalline nanoparticle, we employ approaches of Wang et al. [60] and Schneider et al. [61] as the basis of our model formulation

$$\begin{aligned}f_{mech}\left(\boldsymbol{\phi},\boldsymbol{\epsilon_{el}},\bar{\epsilon}_{pl}\right)&=\frac{1}{2}\left(\boldsymbol{\epsilon}-\boldsymbol{\epsilon}^*\right):\left[\sum_{\alpha\in s}\boldsymbol{C}^{\boldsymbol{\alpha}}\phi^{\alpha}\right]:\left(\boldsymbol{\epsilon}-\boldsymbol{\epsilon}^*\right)\\&+\frac{1}{2}\sum_{\alpha\in s}H^{\alpha}\bar{\epsilon}_{pl}^2\phi^{\alpha},\end{aligned} \tag{14}$$

where $\boldsymbol{C}^{\boldsymbol{\alpha}}$ denotes the phase-dependent stiffness, H^{α} the phase-dependent hardening modulus, and $\bar{\epsilon}_{pl}$ the accumulated plastic strain. The total strain $\boldsymbol{\epsilon}$ is defined as the symmetric part of the displacement gradient $\boldsymbol{\epsilon}=\left[\nabla\boldsymbol{u}+(\nabla\boldsymbol{u})^T\right]/2$. The non-elastic strain $\boldsymbol{\epsilon}^*$ is the sum of eigenstrain and plastic strain $\boldsymbol{\epsilon}^*=\widetilde{\boldsymbol{\epsilon}}(\boldsymbol{\phi})+\boldsymbol{\epsilon_{pl}}$.

In addition, a two-step return mapping algorithm [61] is used to solve mechanical equilibrium in this work. First, a purely elastic predication step is performed where the phase-field microelasticity theory [60] is used to calculate the strain and stress distribution in the solid–liquid coexistence systems [66]

$$\frac{\partial\epsilon_{ij}^0(\boldsymbol{r},t)}{\partial t}=-L_{ijkl}\frac{\partial E^{inhom}}{\partial\epsilon_{kl}^0(\boldsymbol{r},t)}, \tag{15}$$

where ϵ_{ij}^0 is the virtual non-elastic strain and L_{ijkl} governs the evolution rate. The elastically and structurally inhomogeneous elastic energy E^{inhom} is defined as

$$\begin{aligned}E^{inhom}=&\frac{1}{2}\int_V\left[C_{ijmn}^0\Delta C_{mnpq}^{-1}(\boldsymbol{r})C_{pqkl}^0-C_{ijkl}^0\right]\\&\times\left[\epsilon_{ij}^0(\boldsymbol{r})-\epsilon_{ij}^*(\boldsymbol{r})\right]\left[\epsilon_{kl}^0(\boldsymbol{r})-\epsilon_{kl}^*(\boldsymbol{r})\right]dr^3\\&+\frac{1}{2}\int_V C_{ijkl}^0\epsilon_{ij}^0(\boldsymbol{r})\epsilon_{kl}^0(\boldsymbol{r})\,dr^3\\&-\bar{\epsilon}_{ij}\int_V C_{ijkl}^0\epsilon_{kl}^0(\boldsymbol{r})\,dr^3+\frac{V}{2}C_{ijkl}^0\bar{\epsilon}_{ij}\bar{\epsilon}_{kl}\\&-\frac{1}{2}\int_{|\boldsymbol{k}|\neq0}n_i\tilde{\sigma}_{ij}^0(\boldsymbol{k})\Omega_{jk}(\boldsymbol{n})\tilde{\sigma}_{\boldsymbol{kl}}^0(\boldsymbol{k})'n_l\frac{d^3k}{(2\pi)^3},\end{aligned} \tag{16}$$

where C_{ijkl}^0 is the homogeneous elastic stiffness. The effective elastic stiffness (interpolated from the phase-inherent elastic stiffness) can be expressed as the sum of a homogeneous elastic stiffness and the modulus variation $C_{ijkl}^{eff}(\boldsymbol{r})=C_{ijkl}^0-\Delta C_{ijkl}(\boldsymbol{r})$. The phase-field microelasticity theory demonstrates that the stress in the elastically homogeneous system is equal to the stress in the original elastically and structurally inhomogeneous system

$$\begin{aligned}\sigma_{ij}(\boldsymbol{r})&=C_{ijkl}^0\left[\epsilon_{kl}(\boldsymbol{r})-\epsilon_{kl}^0(\boldsymbol{r})\right]\\&=\left[C_{ijkl}^0-\Delta C_{ijkl}(\boldsymbol{r})\right]\left[\epsilon_{kl}(\boldsymbol{r})-\epsilon_{kl}^*(\boldsymbol{r})\right].\end{aligned} \tag{17}$$

The second step is plastic yielding [61], where the Prandtl–Reuss model is used to determine whether the region is yielded plasticly or not

$$f\left(\boldsymbol{\sigma}(\boldsymbol{r}),\bar{\epsilon}_{pl}(\boldsymbol{r})\right):=\|\boldsymbol{\sigma}'(\boldsymbol{r})\|-\sqrt{\frac{2}{3}}\left(f_y(\boldsymbol{\phi})+H(\boldsymbol{\phi})\bar{\epsilon}_{pl}(\boldsymbol{r})\right)\leq0. \tag{18}$$

If the norm of the deviatoric part of the von Mises stress

$$\|\boldsymbol{\sigma}'\|=\|\boldsymbol{\sigma}-\frac{1}{3}\left(\sigma_{11}+\sigma_{22}+\sigma_{33}\right)\boldsymbol{\mathcal{I}}\| \tag{19}$$

exceeds the sum of the yield stress $f_y(\boldsymbol{\phi})$ and the hardening part $H(\boldsymbol{\phi})\bar{\epsilon}_{pl}(\boldsymbol{r})$, the materials will begin to deform plastically

$$\frac{\partial\boldsymbol{\epsilon_{pl}}(\boldsymbol{r},t)}{\partial t}=\dot{\gamma}(\boldsymbol{r})\frac{\partial f\left(\boldsymbol{\sigma}(\boldsymbol{r}),\bar{\epsilon}_{pl}\right)}{\partial\boldsymbol{\sigma}(\boldsymbol{r})}, \tag{20}$$

where $\boldsymbol{\mathcal{I}}$ is the unit determinant and $\dot{\gamma}(\boldsymbol{r})$ the magnitude of plastic flow.

2.2. Modeling and calculation

The thermal stability of Cu–Li–Sn ternary phases has been investigated by Zhang et al. [26] through ab-initio calculations which resulted in the phase diagram for $\mathbf{Cu_xLi_ySn}$ phases, as shown in Fig. 1(a). We investigate the following lithiation process for a polycrystalline nanoparticle

$$\mathbf{Cu_xLiSn}+(y-1)\left(\mathrm{Li}^{+}+e^{-}\right)\rightarrow\mathbf{Cu_xLi_ySn}, \tag{21}$$

where the phases in the initial state of the nanoparticle are arranged in the tuple

$$\mathbf{Cu_xLiSn}=\left\{\mathrm{LiSn},\mathrm{CuLi_2Sn_2},\mathrm{Cu_2LiSn},\mathrm{Cu}\right\}, \tag{22}$$

and all phases include lithium-rich phases are

$$\mathbf{Cu_xLi_ySn}=\left\{\mathbf{Cu_xLiSn},\mathrm{Li_7Sn_3},\mathrm{CuLi_2Sn}\right\}. \tag{23}$$

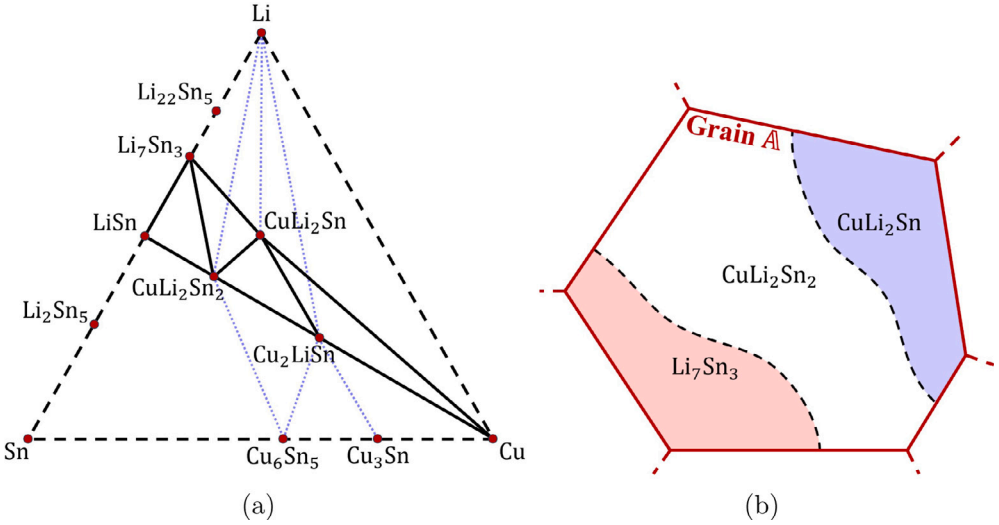

Fig. 1. (a) Calculated Cu–Li–Sn phase diagram at 0 K [26]; (b) Schematic diagram for transformation of $CuLi_2Sn_2$ phase to Li_7Sn_3 and $CuLi_2Sn$ phases in grain $\mathbb{A}$.

2.2.1. Modeling multiphase transformation in a single grain

For the sake of clearly understand the modeling of multiphase transformation in polycrystalline nanoparticle, we arrange all grains into tuple $\mathcal{G}=\{\mathbb{A},\mathbb{B},\mathbb{C},\dots\}$. And the volume fraction of the solid phase can be considered as the sum of all grains

$$\phi^s = \phi^{\mathcal{G}} = \sum_{\mathbb{A}\in\mathcal{G}} \phi^{\mathbb{A}}. \tag{24}$$

As shown in Fig. 1(b), the transition process for $\mathbf{Cu_xLi_ySn}$ phases occurs separately within each grain, and the sum of these phases volume fractions is equal to the volume fraction of the grain

$$\phi^{\mathbb{A}} = \sum_{\alpha\in\mathbf{Cu_xLi_ySn}} \phi^{\mathbb{A},\alpha}, \tag{25}$$

e.g. the transformation of $CuLi_2Sn_2$ phase to Li_7Sn_3 and $CuLi_2Sn$ phases in grain $\mathbb{A}$ during lithiation process. In addition, the grain boundaries do not evolve during the simulation.

The eigenstrain due to lithiation can be computed from the changes in molar volumes [51]

$$\widetilde{\epsilon}(\boldsymbol{\phi}) = \phi^s\widetilde{\epsilon}_0 + \sum_{\alpha\in s}\phi^\alpha\widetilde{\epsilon}^\alpha, \tag{26}$$

where $\widetilde{\epsilon}_0$ can be understood as the homogeneous eigenstrain remaining from the charging/discharging history, and $\widetilde{\epsilon}^\alpha$ is the phase-dependent eigenstrain

$$\widetilde{\epsilon}^\alpha = \left[\left(\frac{V_m^\alpha}{V_m^0}\right)^{\frac{1}{3}} - 1\right]\boldsymbol{I}, \tag{27}$$

where V_m^α represents the molar volume of phase α, and V_m^0 the reference molar volume.

2.2.2. Modeling polycrystalline nanoparticle

Tin electrode suffers from rapid degradation due to the large volume changes during cycling. For the first time, Zhou et al. [13] used focused ion beam (FIB) polishing and scanning electron microscopy (SEM) imaging techniques to monitor the microstructural evolution of individual tin particle at micrometer scale by in-situ FIB-SEM during electrochemical cycling, as shown in Fig. 2. In Fig. 2(a), the voltage profile of the first cycle (blue line) and the estimated relative volume (orange triangle symbol) at different states of discharge/charge can be observed. Fig. 2(b) shows the SEM image of particle before discharging. And Fig. 2(c–g) is the SEM images at 20%, 40%, 60%, 77% and 100% of lithiation process.

In order to model such an electrode particle similar to the work of Zhou et al. we construct non-ideal spherical polycrystalline nanoparticles in three-dimensional (a computational cell of 128 × 128 × 128) and two-dimensional (a computational cell of 256 × 256) spaces, respectively. As shown in Fig. 3(a), 100 grains are generated in the 3D nanoparticle. In Fig. 3(b–e), four 2D nanoparticles with 200 grains are shown. It should be noted that the grain distribution is same in all four 2D nanoparticles at the initial state and during lithiation, but the phase distribution is different. Starting from such complex polycrystalline nanoparticles, we conduct charging simulations which are governed by the following dynamic processes:

- **Phase transformation:** As the lithium concentration within the electrode rises, the lithium-rich phase will precipitate and grow. In some existing work [51,67], the lithium-rich phase usually grows from the surface of the electrode to the interior.
- **Bulk kinetics:** Both phase transitions and the surface reaction are strongly coupled to the bulk diffusion behavior which is driven by the diffusion potential.
- **Lithiation:** The local rate of electrochemical reaction on the electrode surface is influenced by the morphology of the electrode, the phase transition and the diffusion pathways. While the local surface reaction is heterogeneous, the total flux is prescribed assuming a constant current charging condition.

Volume change plays a crucial role during the investigation of Sn-based nanoparticles, impacting their morphology, distribution of components and energy density through expansion, contraction and the occurrence of cracks. In our previous attempt to model Sn-based particles [51], the effects of all three are taken into account. The lithiation rate was converted to the volume change rate, leading to the growth of the electrode, which is similar to the electrodeposition model published by Chen et al. [68]. It is well known that an increase in particle volume results in a decrease in lithium concentration (based on the principle of mass conservation), while the electrode reaction (Eq. (4)) leads to an increase in lithium concentration. Therefore, after considering nanoparticle volume changes, the voltage calculation (Eqs. (28) and (29)) in this work will become even more unstable, which is one simulation limitation. Moreover, from the modeling experience of other researchers [46,48,66,69], the phase-field model is a numerical model that describes the evolution of phase interface, which makes it difficult to describe volume changes within the phase. It means that in the classical total energy framework, the phase-field model cannot accurately describe the expansion of lattices and grains inside the nanoparticle. This is another simulation limitation. Therefore, in this work, the effect of the lithiation process on the volume of the nanoparticle is not considered.

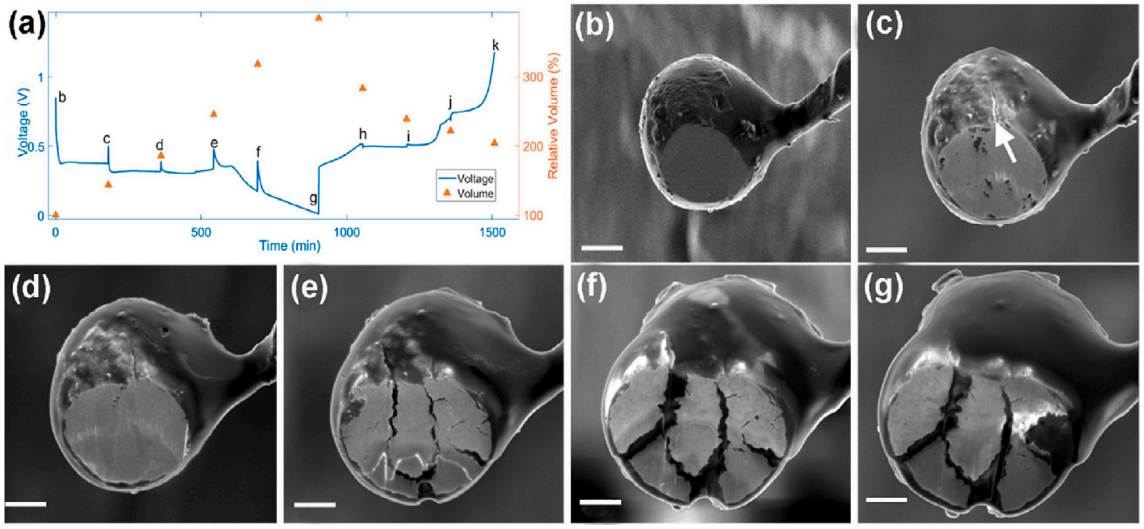

Fig. 2. A Sn nanoparticle with 10 μm diameter fully discharged/charged at 0.3 nA (about C/15 rate). (a) Voltage profile and relative volume of the first cycle. (b–g) SEM images of Sn nanoparticle at 0%, 20%, 40%, 60%, 77% and 100% of discharge states respectively.
Source: Reprinted (adapted) with permission from Ref. [13].

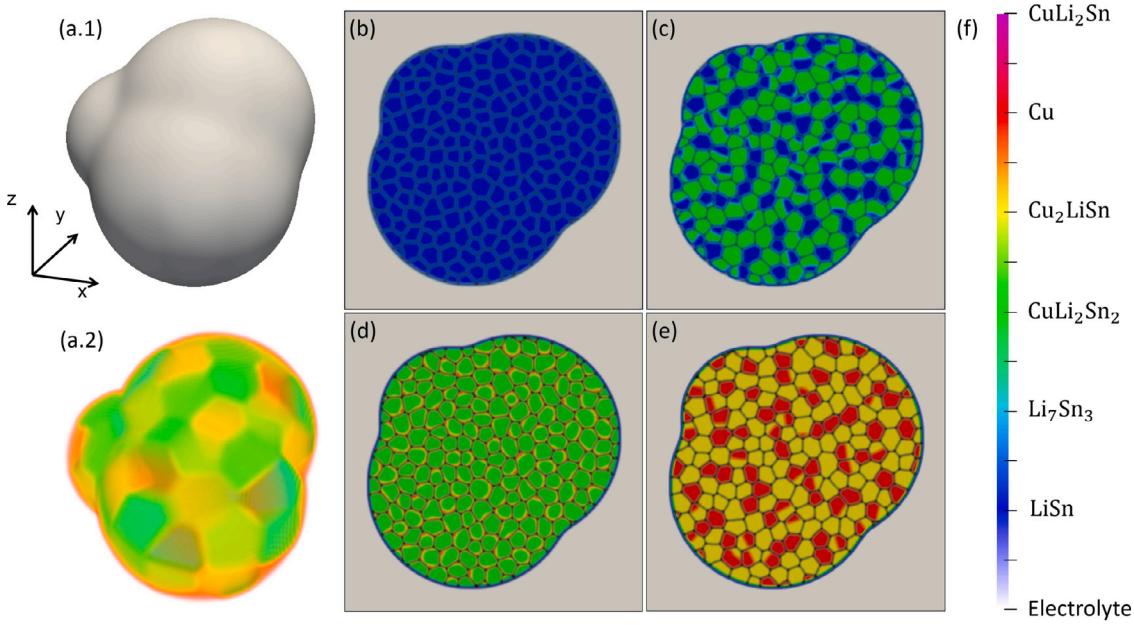

Fig. 3. Fabrication of polycrystalline nanoparticles (grains are distinguished by color in 3D and the black grid in 2D): (a.1) Shape of 3D nanoparticle, (a.2) Grains distribution within 3D nanoparticle, (b) 2D nanoparticle with LiSn phase, (c) 2D nanoparticle with LiSn and $CuLi_2Sn_2$ phases, (d) 2D nanoparticle with $CuLi_2Sn_2$ and Cu phases, and (e) 2D nanoparticle with Cu_2LiSn and Cu phases. The phase distribution in 2D nanoparticles is generated by spinodal decomposition method (see Supplementary Material). In addition, (f) is the color bar used to characterize each phases.

First, the simulation results for the Sn polycrystalline nanoparticle in 3D will be compared to the experimental voltage data (as shown in Fig. 2(a)). Afterwards, the effect of Cu doping in Sn electrodes is discussed based on 2D simulation studies.

2.2.3. Operate voltage calculation

Generally, pure lithium is chosen as another electrode in the full cell in experiments [13,70]. The operate voltage (V) of this full cell can be calculated by the following equation [71]

$$V = -\frac{\mu_{\mathrm{Li}}^{\mathrm{pos}} - \mu_{\mathrm{Li}}^{\mathrm{neg}}}{\mathscr{F}}, \tag{28}$$

where $\mu_{\mathrm{Li}}^{\mathrm{pos}}$ and $\mu_{\mathrm{Li}}^{\mathrm{neg}}$ are the electrochemical potentials of lithium in the cathode and anode. Pure lithium is considered as the anode in this battery, and its chemical potential is a constant value. On the cathode side, the overpotential depends on the chemical potential of lithium at the surface of the Cu_xLi_ySn polycrystalline nanoparticle. However, to avoid the effect of numerical instability at the electrode surface, the electrochemical potential of the lithium within the whole nanoparticle is counted with the help of μ_{Li}^{s} calculation equation in local

$$\mu_{\mathrm{Li}}^{s} = f_{bulk}^{s} + \widetilde{\mu}_{\mathrm{Li}}^{s}\left(1 - x_{\mathrm{Li}}\right) - \widetilde{\mu}_{\mathrm{Cu}}^{s} x_{\mathrm{Cu}}. \tag{29}$$

2.2.4. Material data for Cu_xLi_ySn system

As defined in Eq. (23), all phases **Cu_xLi_ySn** involved in this work are stoichiometric compounds (compounds with a very narrow composition range or compounds that strictly adhere to stoichiometry). The thermodynamic model of a stoichiometric compound is constructed based on

Table 1
Formation energies [26,72] of phases considered in this work.

Phases	Formation energy (kJ mol^{-1})
LiSn	−33.31
$CuLi_2Sn_2$	−32.595
Cu_2LiSn	−20.776
Li_7Sn_3	−39.62
$CuLi_2Sn$	−33.23

Reference states [73] are FCC-Cu, BCC-Li and BCT-Sn.

the fundamental assumption of the fixed component ratio and its Gibbs free energy function is independent of the concentration. To enable the use of the energies of stoichiometric compounds in phase-field simulations, the common approach is to assume that stoichiometric compounds also have a certain solubility [51] and to construct a numerical chemical energy model

$$f^{\alpha}_{chem}\left(\boldsymbol{x}^{\alpha},T\right)=A\sum_{i=1}^{K-1}\left(x_i^{\alpha}-x_{i,eq}^{\alpha}\right)^2+\left(V_m\right)^{-1}G_m^{\alpha}\left(T\right), \tag{30}$$

where A is related to the solubility magnitude, $x_{i,eq}$ the stoichiometric ratio of the component i in stoichiometric component, V_m represents the molar volume, and G_m^{α} the Gibbs energy of the stoichiometric compound α. Generally, G_m^{α} can be evaluated by the formation energy ΔG_m^{α} (as shown in Table 1) and the reference state energy of corresponding elements $G_m^{\mathrm{REF-i}}$

$$G_m^{\alpha}\left(T\right)=\Delta G_m^{\alpha}+\sum_{i}^{K}G_m^{\mathrm{REF-i}}\left(T\right)x_{i,eq}^{\alpha}. \tag{31}$$

Inserting Eq. (30) to Eq. (11), the diffusion potential of component i in α phase can be derived

$$\tilde{\mu}_i^{\alpha}=\frac{\partial f_{bulk}^{\alpha}}{\partial x_i^{\alpha}}=2A\left(x_i^{\alpha}-x_{i,eq}^{\alpha}\right). \tag{32}$$

One basic assumption of the grand-potential formulation is that the diffusion potential is continuously distributed at the phase interface $\tilde{\mu}_i^{\alpha}=\tilde{\mu}_i^{\beta}=\cdots=\tilde{\mu}_i$, which means that the phase-dependent concentration can be calculated directly from the diffusion potential

$$x_i^{\alpha}\left(\tilde{\boldsymbol{\mu}},T\right)=\frac{\tilde{\mu}_i}{2A}+x_{i,eq}^{\alpha}. \tag{33}$$

Moreover, the partial difference of the phase-dependent concentration with respect to the diffusion potential, which is needed in Eq. (3), is given by

$$\chi_{ij}^{\alpha}\left(\tilde{\boldsymbol{\mu}},T\right)=\frac{\partial x_i^{\alpha}\left(\tilde{\boldsymbol{\mu}},T\right)}{\partial\tilde{\mu}_j}=\delta_{ij}\frac{1}{2A}, \tag{34}$$

where δ_{ij} is the Kronecker Delta.

For the eigenstrain model (see Eqs. (26) and (27)), the molar volume of each solid phase is required. It is considered that the total amount of inactive substances (Cu and Sn) within the nanoparticle remains constant during the lithiation process. The crystal structure and corresponding molar volume of each $Cu_xLi_ySn_{6-x}$ phase are listed in Table 2.

More simulation parameters and material data of Cu_xLi_ySn nanoparticle can be observed in Appendix B.

3. Implementation and optimization

The presently developed phase-field model is implemented in the self-developed open-source parallel solvers package MInDes, which is uploaded to github [74] and introduced in detail in the Supplementary Material. Fig. 4 illustrates the framework of the MInDes package. The body of the program is the evolution of the phase, concentration, and temperature fields. And the other multiphysics fields (e.g., mechanical, flow, electric, magnetic, etc.) belong to the external fields

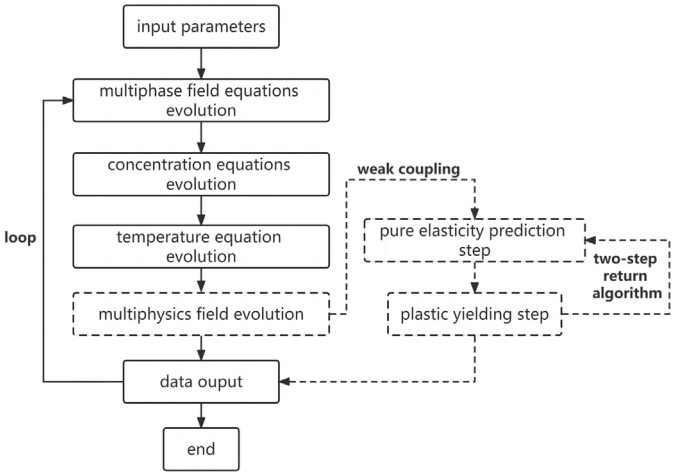

Fig. 4. Flowchart of MInDes (Microstructure Intelligent Design) phase-field simulation package.

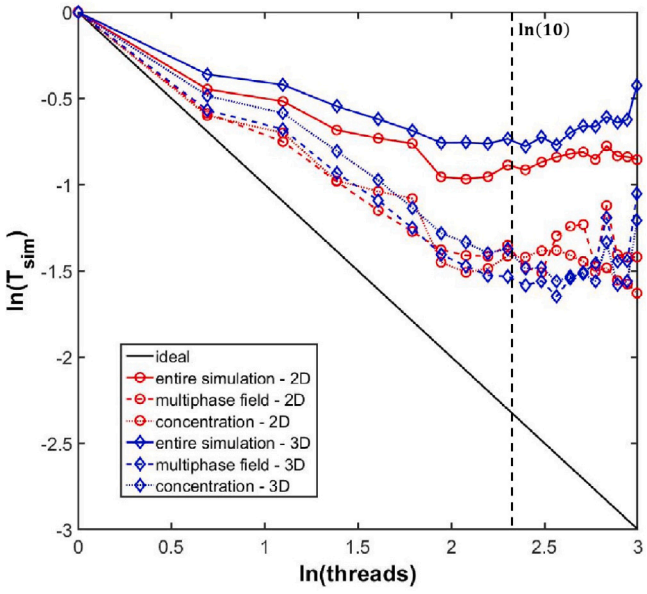

Fig. 5. Time consumed for computing 1000 simulation steps of 2D nanoparticle (red line) and 20 simulation steps of 3D nanoparticle (blue line) by using OpenMP acceleration. The horizontal axis is the natural logarithm of the thread count, and the vertical axis is the natural logarithm of the normalized simulation time $T_{sim}=T_{multiple}/T_{single}$ (divide the multi-threaded simulation time by the single-threaded time). Among them, the solid lines represent the entire simulation time consumed, the dotted lines represent the time consumed for the evolution of concentration equations, and the dashed lines represent the time consumed for the evolution of multiphase field equations. The black solid line represents the ideal scale.

can be optionally invoked. The governing equations (3) and (13) are discretized in space with the finite difference scheme and in time with the explicit Euler method. In this work, we consider a two-step return algorithm to solve the elastoplastic stress distribution. In the purely elastic prediction step, Eq. (15) is solved by the semi-implicit Fourier spectral method. In the plastic yielding step, we solved Eq. (20) by finite difference method.

For the sake of a high efficiency, we optimize modeling and simulation. Merging the order parameters of non-contacting grains to reduce the amount of stored fields is a very effective treatment to save memory consumption and improve computational efficiency. As mentioned above, nanoparticles containing 100 grains in 3D and 200 grains in 2D are prefabricated, and they consume 43.44 gigabyte (GB)

Table 2
Lattice constants (nm) and Molar volume (10^{-5} m^3/mol) of each phase.

Phases	Space group	a	b	c	Molar volume	Remark
Cu_6	$Fm\bar{3}m$	0.358	2.148	0.358	4.134	[73]
Li_6Sn_6	$I4_1/amd$	0.4421	2.6526	2.5889	15.24	[72]
$Cu_2Li_4Sn_4$	$I4_1/amd$	0.4464	0.8928	1.9524	11.7	[26]
$Cu_4Li_2Sn_2$	$P6_3/mmc$	0.4329	0.8658	0.7679	7.504	[26]
$Li_{14}Sn_6$	$P2_1/m$	0.9462	1.714	0.4726	22.2	[72]
$Cu_3Li_6Sn_3$	$F\bar{4}3m$	0.6323	1.8969	0.6323	11.412	[26]

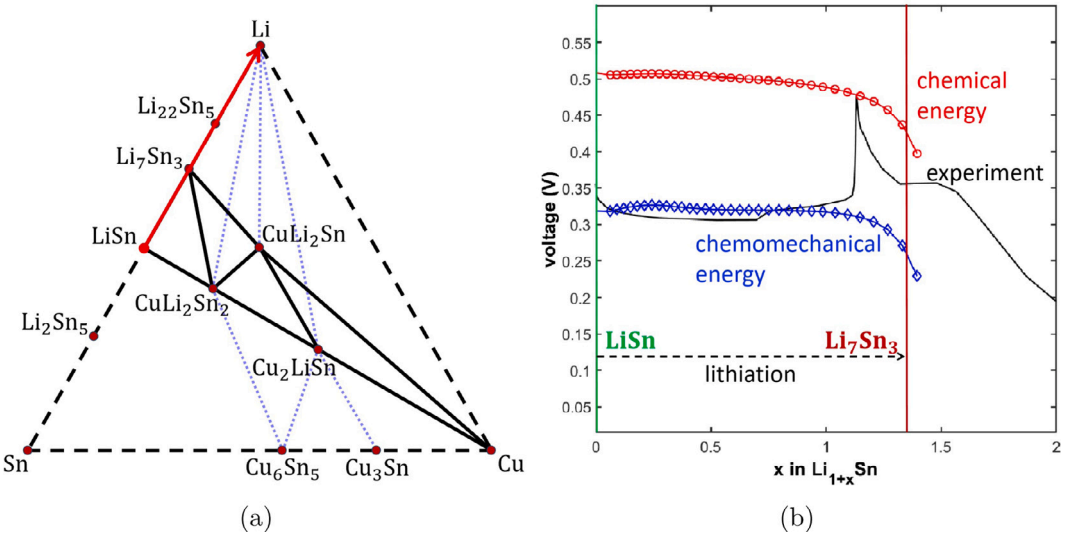

Fig. 6. Lithiation process of Li_xSn 3D nanoparticle: $3LiSn + 4\left(Li^+ + e^-\right) \rightarrow Li_7Sn_3$. (a) Phase transition pathways (red arrow) for nanoparticle during lithiation process. (b) The voltage profile obtained from the simulation (solid red and blue lines) is compared with the experimental one (solid black line).

and 2.63 GB of computational memory, respectively. During the optimization process, 100 grains within the 3D nanoparticle are merged into 9 order parameters and the memory consumption is reduced to 5.32 GB. Similarly, the 200 grains within the 2D nanoparticles are parametrized by 6 order parameters to reduce the memory consumption to 0.11 GB. Then the data structures of LiSn and Li_7Sn_3 phases are constructed in each grain in 3D nanoparticles, and the memory consumption finally reached 11.69 GB during lithiation process. The data structures of $\mathbf{Cu_xLi_ySn}$ phases are constructed in each grain in 2D nanoparticles, and the memory consumption reaches 1.49 GB during lithiation process (discussed in detail in the Supplementary Material). During the simulations, we use Open Multi-Processing (OpenMP) [75] to accelerate the computation of Eqs. (3), (6), (13), (15), and (20). As shown in Fig. 5, the time consumed to calculate 1000 simulation steps for 2D nanoparticle (blue line) and 20 simulation steps for 3D nanoparticle (orange line) is counted, where the solid lines are the total time consumed, the dashed and dotted lines are the time consumed for Eqs. (3) and (13), respectively. This work is carried out based on 13th Generation Intel Core i9-13900K and 64 GB of RAM, and according to Fig. 5 it can be determined that the optimal number of parallel threads is 10 in this environment.

4. Result and discussion

In the following section, the equations and polycrystalline model are validated qualitatively and quantitatively using Li_xSn 3D nanoparticle experimentally observed [13]. Subsequently, the effect of Cu doping in Li_xSn nanoparticles on their mechanical properties is investigated.

4.1. Lithiation process of Li_xSn 3D nanoparticle

In their review, Gao et al. [71] come to the conclusion that the nano-size effects have a significant influence on the voltage profile, the additional energy is caused by strain, surface or interface energy, or Li^+ concentration gradient in the diffuse interface. In our previous work [51], we discussed the difference in the voltage plateau formed by the equilibrium of each two phases during the multiphase transition and by the overall and localized expansions of spherical nanoparticle brought about by the phase transition. Therefore, based on these existing studies, we can verify the accuracy of the energy density, diffusion potential, and stress–strain distribution during the simulation process mainly by comparing the calculated voltage profiles with the experimental ones [13].

The red arrow in Fig. 6(a) represents the phase transition path during the lithiation of 3D polycrystalline nanoparticle, namely $3LiSn + 4\left(Li^+ + e^-\right) \rightarrow Li_7Sn_3$. In Fig. 6(b), the black curve corresponds to the voltage profile measured experimentally, which can be obtained from Fig. 2(a). The red curve displays the voltage profile calculated only considering chemical energy, and the blue curve is the voltage profile calculated considering chemomechanical energy. As the Li_xSn nanoparticle accumulates strain during the lithiation process, the energy density within the bulk phase is increased which results in a shift of the calculated voltage plateau. This is consistent with the conclusions drawn by Zhang et al. [26,72]. It is worth mentioning that the observed "peak" in black curve (as well as the "peaks" in Fig. 2(a)) are related to their experimental methods. Before imaging Sn nanoparticle by a scanning electron microscope (SEM), Zhou et al. [13] polish the nanoparticle with the help of focused ion beam (FIB). This will lead to fluctuations of the voltage profile, resulting in the appearance of peaks. Since there is no polishing step in the simulation process, there are no peaks. The mechanical analysis of the electrode nanoparticle and the comparison of the simulated voltage profile with the experimental one allow us to obtain a more accurate distribution of the mechanical energy density, stresses and strains.

Fig. 7 illustrates the phase transition during lithiation in the Li_xSn 3D nanoparticle, where the dark blue phase is LiSn and the light

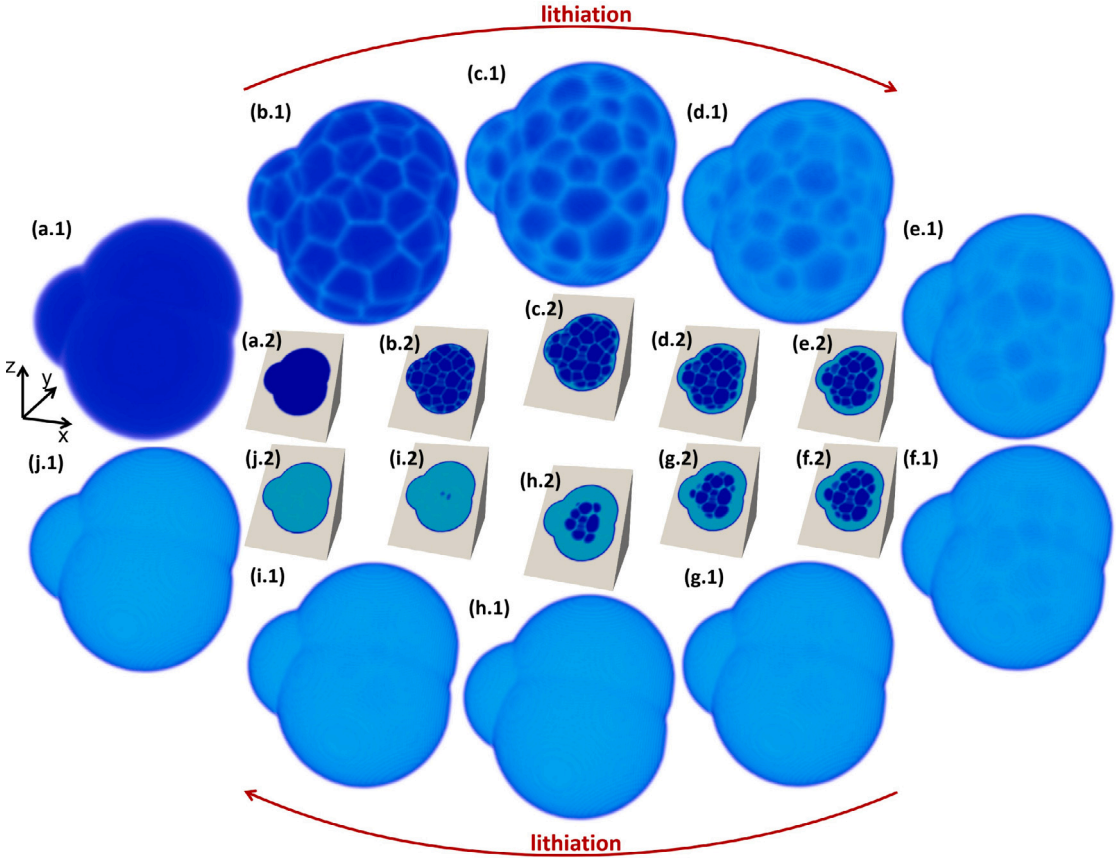

Fig. 7. Lithiation process of Li_xSn 3D nanoparticle, where simulation time (a) at 0 s (second); (b) at 1511.6 s; (c) at 3031.6 s; (d) at 4556.6 s; (e) at 6085 s; (f) at 7612 s; (g) at 9139 s; (h) at 10 665 s; (i) at 12 201.7 s; (j) at 12 578.4 s. The series of graphs labeled 1 shows the phase distribution on a semi-transparent nanoparticle. The series of graphs labeled 2 shows the phase distribution inside the nanoparticle. The colorbar is consistent with Fig. 3(f), where the dark blue phase is LiSn and the light blue phase is Li_7Sn_3.

blue phase is Li_7Sn_3. Graphs (a–j) represent the phase distributions at 0, 1511.6, 3031.6, 4556.6, 6085, 7612, 9139, 10 665, 12 201.7, and 12 578.4 s during the lithiation process, respectively. The series of graphs labeled 1 shows the phase distribution on a semi-transparent nanoparticle. The series of graphs labeled 2 shows the phase distribution inside the nanoparticle. Firstly, it can be observed that the Li_7Sn_3 phase precipitates from the surface as well as the internal grain boundaries of the nanoparticle (in Fig. 7(b1) and (b2)), then a large amount of Li_7Sn_3 phase gradually precipitates from the surface layer of the nanoparticle (as shown in Fig. 7(c) and (d)), and finally the Li_7Sn_3 phase grows towards the interior of the particles (in Fig. 7(e–j)).

Fig. 8 illustrates the distribution of von Mises stresses during lithiation of Li_xSn 3D nanoparticle, where the phase structures corresponding to graphs (a–j) are shown in Fig. 7(a–j), respectively. The series of graphs labeled 1 shows the von Mises stress distribution on a semi-transparent nanoparticle. The series of graphs labeled 2 shows the von Mises stress distribution inside the nanoparticle. It can be seen that as the Li_7Sn_3 phase precipitates, the von Mises stress reaches a maximum near the interface between the Li_7Sn_3 phase and the LiSn phase. When the Li_7Sn_3 phase precipitates and covers the surface of the nanoparticles during the lithiation process (Fig. 7(c) and (d)), the maximal von Mises stresses can be calculated on the nanoparticle surface (Fig. 8(c) and (d)). Then, as the Li_7Sn_3 phase grows, the phase interface between LiSn and Li_7Sn_3 phases moves towards the interior of the nanoparticle, and the region with the highest von Mises stress also moves towards the interior of the nanoparticle, and its value decreases gradually. This represents the fact that cracks are more likely to be generated on the nanoparticle surface when the lithium-rich phase starts to precipitate, and the form of crack growth tends to propagate from the nanoparticle surface to the interior, which was demonstrated experimentally by Eom et al. [76] and Ying et al. [77]. And Liu et al. used *in situ* transmission electron microscopy to study the lithiation process of individual Si nanoparticle in real time and discussed the stress distribution in it, which can also be applicable to the understanding of stress distribution and crack generation during lithiation in Sn-based nanoparticles [4]. Moreover, as shown in Fig. 8(b) and (c), the cracks on the surface of the nanoparticle are more likely to propagate along the grain boundaries, which is consistent with the conclusions drawn by Wang et al. [20] and laterally illustrates the regularity of the crack distribution in Fig. 2(e). Additional 2D sections from different locations of the 3D nanoparticle are illustrated in Figs. S17–S20 in the Supplementary Material.

To gain a deeper understanding of the lithiation process in the Li_xSn 3D nanoparticle, the calculated results at 9139 s are further analyzed. The corresponding phase distributions of LiSn and Li_7Sn_3 are shown in Fig. 9(b), the distribution of lithium diffusion potential, chemical energy density, and chemomechanical energy density are shown in Fig. 9(c), (d), and (e), respectively. In order to demonstrate the energy information more clearly, the data within the nanoparticle is obtained along the *y*-direction (in graphs (c), (d), and (e)) to plot in Fig. 9(a), where the black line is the diffusion potential, the blue line is the chemomechanical energy density, and the red line is the chemical energy density. Obviously, the energy density after considering the contribution of mechanical energy is relatively higher, which also results in a higher chemical potential of lithium calculated by Eq. (29), and therefore to a lower output voltage [26,72].

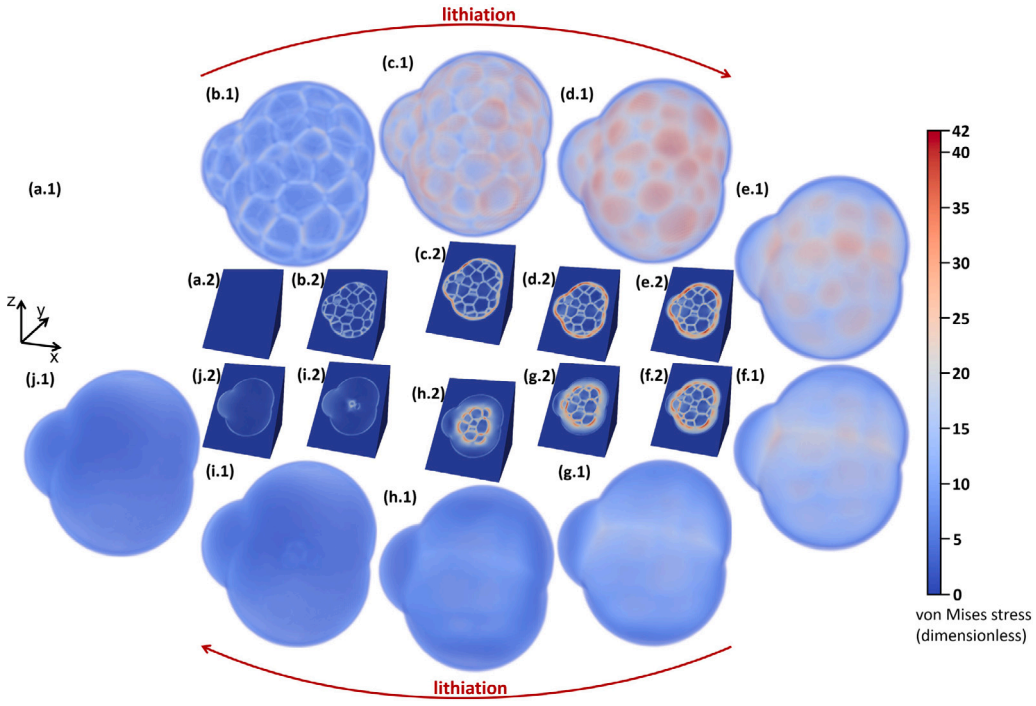

Fig. 8. Lithiation process of Li_xSn 3D nanoparticle, where simulation time (a) at 0 s; (b) at 1511.6 s; (c) at 3031.6 s; (d) at 4556.6 s; (e) at 6085 s; (f) at 7612 s; (g) at 9139 s; (h) at 10 665 s; (i) at 12 201.7 s; (j) at 12 578.4 s. The series of graphs labeled 1 shows the von Mises stress distribution on a semi-transparent nanoparticle. The series of graphs labeled 2 shows the von Mises stress distribution inside the nanoparticle.

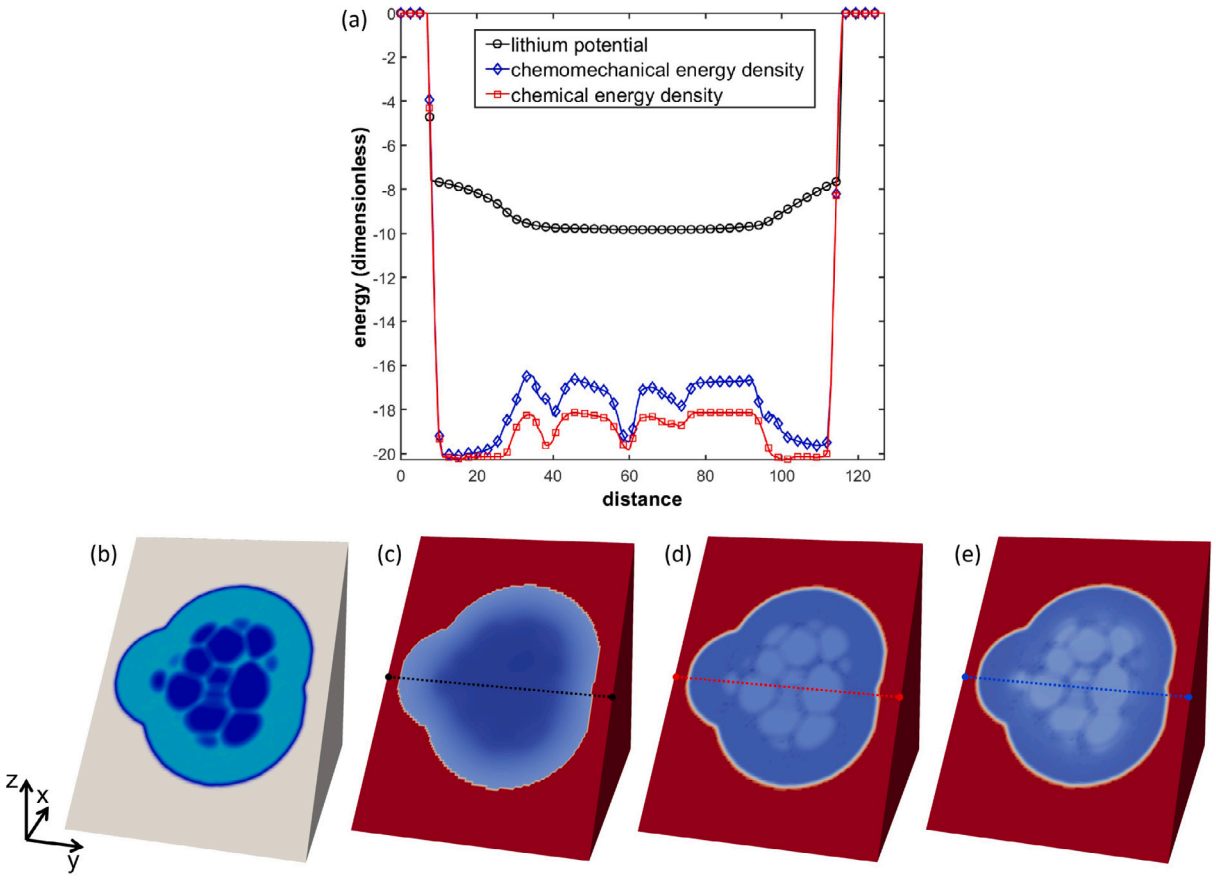

Fig. 9. The Li_xSn 3D nanoparticle charge for 9139 s: (a) lithium diffusion potential (black line), chemomechanical energy density (blue line), and chemical energy density (red line) distribution obtained from graphs (c), (d) and (e); (b) phase distribution; (c) diffusion potential of lithium; (d) chemical energy density distribution; (e) chemomechanical energy density distribution. The colorbar for graph (b) is consistent with Fig. 3(f).

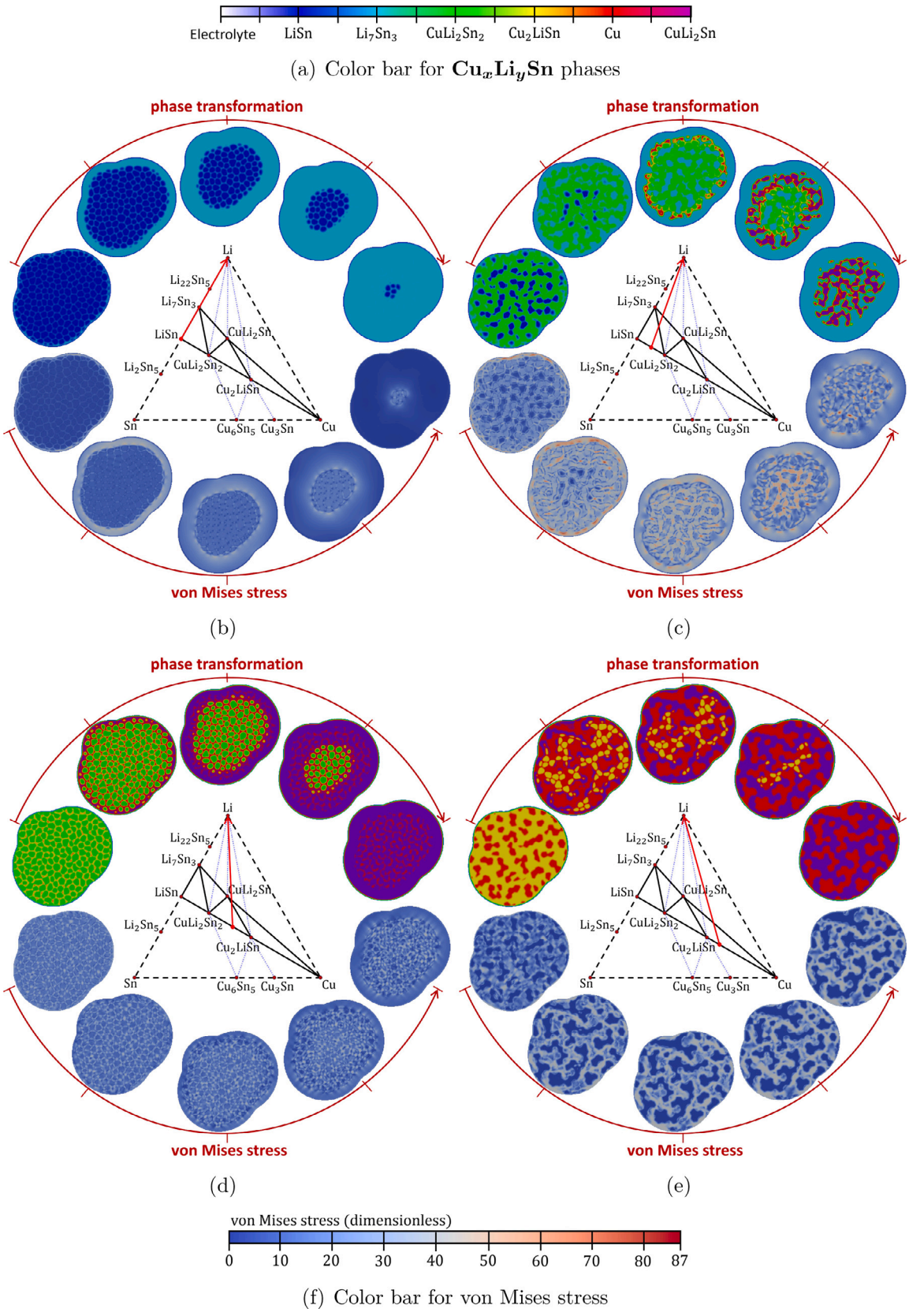

Fig. 10. Lithiation process of Cu_xLi_ySn 2D nanoparticle: phases and von Mises stress distribution during lithiation of nanoparticle with initial grains occupied by (b) LiSn phase; (c) LiSn and $CuLi_2Sn_2$ phases; (d) $CuLi_2Sn_2$ and Cu phases; (e) Cu_2LiSn and Cu phases.

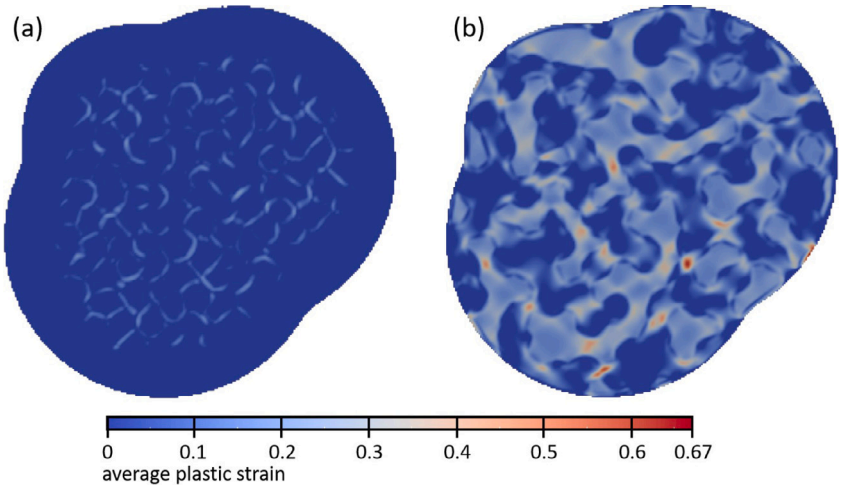

Fig. 11. Average plastic strain distribution of Cu_xLi_ySn nanoparticle with initial grains occupied by (a) $CuLi_2Sn_2$ and Cu phases, and (b) Cu_2LiSn and Cu phases after lithiation.

4.2. Lithiation process of Cu_xLi_ySn 2D nanoparticle

Many researchers demonstrated that copper doping can effectively improve the mechanical property and cyclability of Sn-based electrodes [20,37,38], but there is a lack of simulations in order to investigate how copper acts as a stress-buffering phase in such complex polycrystalline structures. In this subsection, we will investigate the variation of mechanical properties of a Cu_xLi_ySn nanoparticle through Cu doping with the guidance of the Cu–Li–Sn phase diagram [26].

Based on the previous validation, phase-field simulations of the multiphase transition of Cu_xLi_ySn polycrystalline nanoparticle during lithiation will be performed in 2D to save the simulation time. Similar to the settings of 3D polycrystalline nanoparticle, the three processes of phase transition, bulk diffusion, and lithiation are also involved in the simulations of 2D polycrystalline nanoparticle. Under the guidance of the Cu–Li–Sn phase diagram, we carried out four simulations in two dimensions with initial concentrations of Cu_0LiSn (as shown in Fig. 10(b)), $Cu_{0.5}Li_2Sn_2$ (as shown in Fig. 10(c)), $Cu_6Li_5Sn_5$ (as shown in Fig. 10(d)) and Cu_3LiSn (as shown in Fig. 10(e)). In Fig. 10, each of the phase diagrams in the center of graphs (a–d) illustrates the phase transition path (red arrow) of each nanoparticle during the lithiation process: (a) $LiSn + Li^+ + e^- \rightarrow Li_7Sn_3$, (b) $LiSn + CuLi_2Sn_2 + Li^+ + e^- \rightarrow Li_7Sn_3 + CuLi_2Sn$, (c) $CuLi_2Sn_2 + Cu + Li^+ + e^- \rightarrow CuLi_2Sn$, and (d) $Cu_2LiSn + Li^+ + e^- \rightarrow CuLi_2Sn + Cu$.

All four lithiation reactions have different phase transition processes. In Fig. 10(b), the Li_7Sn_3 phase precipitates on the surface of LiSn polycrystalline nanoparticle and grows toward the interior of the particle in the same way as the 3D lithiation process. In Fig. 10(c), the first process is the transformation of LiSn phase into the Li_7Sn_3 phase, and when LiSn phase disappears, $CuLi_2Sn_2$ phase will then transform into Li_7Sn_3 and $CuLi_2Sn$ phases. In Fig. 10(d), $CuLi_2Sn_2$ phase will transform to $CuLi_2Sn$ phase after lithiation, and some Cu will be consumed in this process, and thus the volume of Cu phase within the nanoparticle is reduced. In Fig. 10(e), Cu_2LiSn phase will transform to $CuLi_2Sn$ phase and a certain amount of Cu will be precipitated, so the volume of Cu phase will increase. The mechanical influence and likelihood for fracture are analyzed by means of the von Mises stress distribution for all four Cu content. In comparison with Cu_0LiSn nanoparticle (Fig. 10(b)), when a small amount of Cu is doped in this nanoparticle without precipitating the Cu phase (Fig. 10(c)), the von Mises stress tends to rise which increases the likelihood for particle damage. This can be verified in the work of Zhang et al. [26], where the back-scattered electron (BSE) images show that cracks are already existing in the annealed Cu_xLi_ySn electrode material. In contrast, the mechanical properties of the nanoparticles are improved when the Cu phase precipitates. The von Mises stress is significantly lower in the areas where the Cu phase exists compared to other regions. The maximal von Mises stresses in Fig. 10(d) and (e) are lower than those in Fig. 10(b) and (c). This indicates that the Cu phase effectively buffers localized stress concentration, which is consistent with the conclusion of Wang et al. [20]. Fig. 11 shows the average plastic strain which is accumulated inside the nanoparticles during lithiation and calculated by the following equation [61].

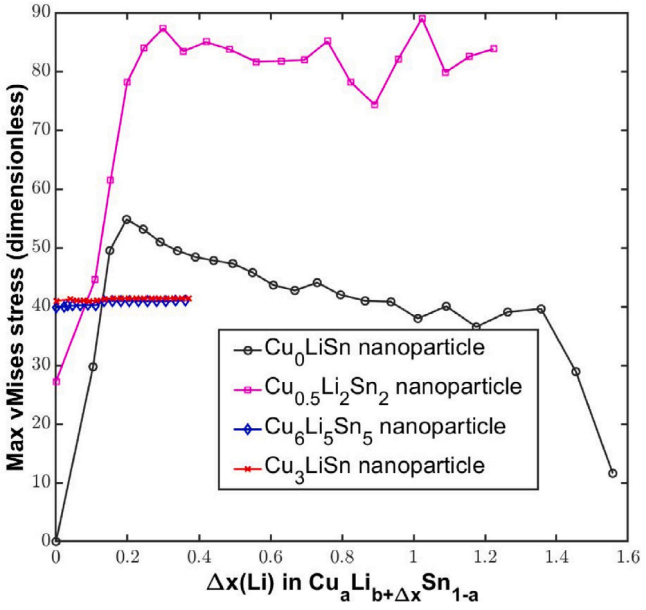

Fig. 12. Maximal von Mises stress with time during lithiation of Cu_xLi_ySn 2D nanoparticles.

$$\frac{\partial \bar{\epsilon}_{pl}(\boldsymbol{r},t)}{\partial t} = \sqrt{\frac{2}{3}}\dot{\gamma}(\boldsymbol{r}). \tag{35}$$

It can be seen that the average plastic strain is mainly distributed in the regions where the Cu phase exists, which also have lowest von Mises stresses due to plastic yielding. This also results in low von Mises stresses for the whole nanoparticles, which avoids material damage and improves their mechanical properties.

Fig. 12 illustrates the variation of maximal von Mises stress within Cu_0LiSn (black curve), $Cu_{0.5}Li_2Sn_2$ (purple curve), $Cu_6Li_5Sn_5$ (blue curve), and Cu_3LiSn (red curve) nanoparticles during lithiation process.

It can be seen that the maximal von Mises stress of Cu_0LiSn nanoparticle is increasing at the early stage of lithiation when Li_7Sn_3 phase precipitates on the surface of nanoparticle. As the transformation proceeds, the maximal von Mises stress gradually decreases. This trend can only be observed in this case because there is only one phase inside the nanoparticle either before or after the lithiation reaction. In other cases, there are two phases inside the nanoparticle. Due to the eigenstrain model in this work is primarily considered to be related to the molar volume of each phase. For a single-phase nanoparticle, there is no stress concentration inside and the maximum von Mises stress is the lowest. Therefore, it indicates that the damage of Cu_0LiSn nanoparticle is more likely to occur in the early stage of lithiation and preferentially starts from the surface. In the $Cu_6Li_5Sn_5$ and Cu_3LiSn nanoparticles, the maximal von Mises stress is significantly lower than the highest values of the maximal von Mises stress curves for Cu_0LiSn and $Cu_{0.5}Li_2Sn_2$ nanoparticles, which illustrates the important role of the Cu phase for buffering stress.

5. Conclusion

In this study, we have developed and efficiently implemented a framework suitable for simulating the lithiation process of polycrystalline nanoparticles with arbitrary geometries within the multi-physics MInDes package. Initially, the framework's validity is established by simulating the lithiation process of a three-dimensional polycrystalline Li_xSn nanoparticle. Subsequently, the lithiation processes of four two-dimensional polycrystalline nanoparticles with different copper contents are simulated. For the Cu_0LiSn nanoparticle, the phase transition path is $LiSn \rightarrow Li_7Sn_3$. For the $Cu_{0.5}Li_2Sn_2$ nanoparticle, the phase transition path involves $LiSn \rightarrow Li_7Sn_3$ and $CuLi_2Sn_2 \rightarrow CuLi_2Sn + Li_7Sn_3$. The $Cu_6Li_5Sn_5$ nanoparticle undergoes the phase transition $CuLi_2Sn_2 + Cu \rightarrow CuLi_2Sn$, while the Cu_3LiSn nanoparticle experiences the phase transition $Cu_2LiSn \rightarrow CuLi_2Sn + Cu$. After performing mechanical analysis on these four lithiation processes, the following conclusions are drawn:

(i) Cracks tend to appear at grain boundaries on the particle surface during the lithiation process of pure Sn nanoparticles, particularly in the early stage of lithium-rich phase precipitation.

(ii) The mechanical properties of the nanoparticle are reduced, and it becomes more susceptible to cracking when small amounts of Cu are doped into the Sn nanoparticle without the precipitation of the Cu buffer phase. This is attributed to the presence of phases with a higher volume expansion in its phase transition path.

(iii) When the percentage of Cu doping in pure Sn nanoparticles exceeds 50%, the Cu buffer phase precipitates, effectively improving the mechanical properties of the nanoparticle during the lithiation process.

Based on these observations and conclusions, the proposed modeling framework can be applied to advance further investigations. In future research, the crack evolution can be simulated using the finite element method, utilizing the simulated nanoparticle structure from this study. Additionally, the model can be used to examine the physical modification of polycrystalline electrodes and analyze their electrochemical and mechanical performance characteristics.

CRediT authorship contribution statement

Qi Huang: Writing – review & editing, Writing – original draft, Visualization, Validation, Software, Resources, Methodology, Investigation, Formal analysis, Data curation, Conceptualization. **Simon Daubner:** Writing – review & editing, Methodology, Conceptualization. **Daniel Schneider:** Writing – review & editing, Methodology. **Xiaoyu Zheng:** Methodology. **Shuhong Liu:** Data curation. **Yong Du:** Writing – review & editing, Supervision, Project administration, Methodology, Funding acquisition. **Britta Nestler:** Writing – review & editing, Methodology.

Declaration of competing interest

The authors declare that they have no known competing financial interests or personal relationships that could have appeared to influence the work reported in this paper.

Data availability

Data will be made available on request.

Acknowledgments

Q. H. is grateful for the scholarship from China Scholarship Council [grant numbers: 202106370123], which supports his research work in KIT, Germany from March 15th, 2022 to September 14th, 2023. This work was supported by the Sino-German Cooperation Group [grant numbers: GZ1528], which is within the Nation Natural Science Foundation of China and Deutsche Forschungsgemeinschaft of Germany. This work contributes to the research performed at CELEST (Center for Electrochemical Energy Storage Ulm-Karlsruhe) and was partially funded by the German Research Foundation (DFG) under Project ID 390874152 (POLiS Cluster of Excellence). Discussions of the results were facilitated through the programme MTET 38.02.01 by the Helmholtz association.

Code availability

The underlying code MInDes for this study is available in Microstructure-Intelligent-Design/MInDes and can be accessed via this link https://github.com/Microstructure-Intelligent-Design/MInDes.

Appendix A. Thermal fluctuation

As discussed in Section 2.2.2, the phase transition is one of the three simulation types in this work. Considering the local phase instability due to thermal fluctuations, which results in the generation of new phases' noise, is an effective numerical method. Therefore, there are two types of thermal fluctuations to be considered: One is the uniform thermal fluctuation $\zeta = \sum_{\alpha<\beta}^{s,s} \phi^\alpha \phi^\beta \cdot D^{\alpha\beta} \cdot A^s$ (as shown in Fig. A.13(b)), the other is the interfacial thermal fluctuation $\zeta = \sum_{\alpha<\beta<\gamma}^{s,s,N} \phi^\alpha \phi^\beta \phi^\gamma \cdot D^{\alpha\beta} \cdot A^s$ (as shown in Fig. A.13(c)), where $D^{\alpha\beta}$ is the distribution function and A^s is the noise amplitude.

However, considering that the grand-potential equation are coupled closely with the phase-field evolution equation, the generation of noise will have a non-negligible artificial effect on the calculation of the diffusion potential. To ensure the accuracy of the evolution of the diffusion potential, some conditions need to be added to limit the thermal fluctuation within each phase. First, it is assumed that thermal fluctuation occurs mainly at grain boundaries. This was demonstrated when prefabricating $\mathbf{Cu_xLi_ySn}$ nanoparticles (Supplementary Material, Fig. S15). The new phases generated by the uniform thermal fluctuation method grow firstly on grain boundaries, too. Secondly, in the $\mathbf{Cu_xLi_ySn}$ multi-phase system, thermal fluctuations are not present in any case in any area. We assume that thermal fluctuations exist when the newly generated phase has a growing driving force

$$D^{\alpha\beta} = \begin{cases} 0 & \Delta^{\alpha\beta} < 0 \\ rand(0,1) & \Delta^{\alpha\beta} > 0, \end{cases} \tag{A.1}$$

where $\Delta^{\alpha\beta} = \left(\partial/\partial\phi^\beta - \partial/\partial\phi^\alpha\right) F_{bulk}$ is already defined in Eq. (13). As shown in Fig. A.13(a), during the lithiation process, the diffusion potential is higher at the particle surface than inside the particle, so the thermal fluctuation mainly exists in the outer layer of the nanoparticle (in Fig. A.13(b,c)). Because there is no driving force to generate the lithium-rich phase inside the particle, there is no thermal fluctuation.

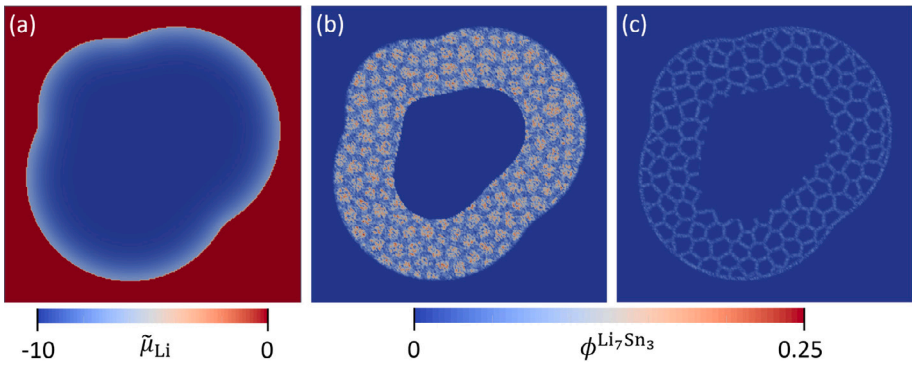

Fig. A.13. Schematic diagram of thermal fluctuation in LiSn phase in each grain ($A^s = 0.25$): (a) distribution of diffusion potential Li, (b) Li_7Sn_3 phase generated by uniform thermal fluctuation, and (c) Li_7Sn_3 phase generated by interfacial thermal fluctuation.

Table B.3
Dimensionless definition and the basic material parameters used in simulation.

Sym.	Description	Expression	Unit	Value	Remark
Δr^*	Size of spatial grid	–	m	5×10^{-8}	–
Δt^*	Time interval	–	s	0.1	–
T^*	Temperature	–	K	300	–
R^*	Molar gas constant	–	J/(mol K)	8.314	–
V_m^*	Molar volume	–	m^3/mol	1×10^{-5}	–
E^*	Energy density	$T^* \times R^*/V_m^*$	J/m^3	2.4942×10^8	–
∂E^*	Interface energy	$E^* \times \Delta r^*$	J/m^2	12.471	–
G^*	Mechanical modulus	E^*	Pa	2.4942×10^8	–
D^*	Diffusivity	$(\Delta r^*)^2/\Delta t^*$	m^2/s	2.5×10^{-14}	–
$\widetilde{L}^{\alpha\beta}$	Interface mobility	–	m/s	5×10^{-4}	–
ϵ	Interface width	–	m	3×10^{-7}	–
D_{Li}	Diffusivity of lithium	–	m^2/s	1×10^{-14}	[78,79]
D_{Cu}	Diffusivity of copper	–	m^2/s	1×10^{-14}	[78,79]
$\gamma^{\alpha\beta}$	Interface energy	–	J/m^2	0.1	[80]
$\widetilde{\gamma}$	Artificial interface energy	–	J/m^2	10.0	[65]
A	Solubility magnitude	–	–	500	–
c_{max}	Full charge lithium	–	–	0.814815	[13]
C-rate	Lithiation rate	–	C	1/15	[13]
$\overline{V}_{grain}$	Average grain size	–	μm^3	0.70058	–

Appendix B. Physical and dimensionless parameters

The dimensionless definition and some of the basic material parameters used in this work are listed in Table B.3. Parameters marked with * are used to transfer the available physical parameters into dimensionless parameters.

Among these parameters, the size of spatial grid Δr is set as 5×10^{-8} m, the time interval Δt is chosen to be 0.1 s. The simulation of lithiation is assumed to occur at a temperature of $T^* = 300$ K, using a molar gas constant of $R^* = 8.314$ J/(mol K), with a standard molar volume of 1×10^{-5} m^3/mol. Therefore, the standard energy density can be calculated by formula $E^* = T^* \times R^*/V_m^*$, similarly, the standard interface energy $\partial E^* = E^* \times \Delta r^*$ and the standard diffusivity $D^* = (\Delta r^*)^2/\Delta t^*$. Due to the equilibrium relationship between the energy density and the external applied forces, which implies that the force per unit area (Pa) equals the energy per unit volume (J/m^3), hence the standard mechanical modulus can be given as $G^* = E^*$. To ensure the stable generation of phase interfaces, the interface energy model $\hat{\gamma}^{\alpha\beta} = \gamma^{\alpha\beta} + \widetilde{\gamma}$ proposed by Schoof et al. [65] is used here, where $\gamma^{\alpha\beta}$ is the interface energy for the materials and $\widetilde{\gamma}$ a special energy to construct a stable diffuse interface. The interface width ϵ is set to be $6 \times \Delta r$. The interface mobility $\widetilde{L}^{\alpha\beta}$ is set as 5×10^{-4} m/s. The numerical chemical energy model is given in Eq. (30), where the solubility magnitude A is given as 500. The diffusivity of lithium and copper in electrode (D_{Li} and D_{Cu}) are set as 1×10^{-14} m^2/s [78,79]. Referring to experimental work [13], the concentration of lithium is 0.814815 (molar fraction) after full charging of the nanoparticle, with a lithiation rate of 1/15 *C-rate*. The average grain size in 3D nanoparticle is 0.70058 μm^3.

References

[1] R.A. Huggins, Lithium alloy negative electrodes, J. Power Sources 81 (1999) 13–19, http://dx.doi.org/10.1016/S0378-7753(99)00124-X.

[2] M. Winter, J.O. Besenhard, Electrochemical lithiation of tin and tin-based intermetallics and composites, Electrochim. Acta 45 (1–2) (1999) 31–50, http://dx.doi.org/10.1016/S0013-4686(99)00191-7.

[3] Y. Zou, Y. Wang, Sn@CNT nanostructures rooted in graphene with high and fast Li-storage capacities, ACS Nano 5 (10) (2011) 8108–8114, http://dx.doi.org/10.1021/nn2027159.

[4] X.H. Liu, L. Zhong, S. Huang, S.X. Mao, T. Zhu, J.Y. Huang, Size-dependent fracture of silicon nanoparticles during lithiation, ACS Nano 6 (2) (2012) 1522–1531, http://dx.doi.org/10.1021/nn204476h.

[5] J. Liu, K. Song, C. Zhu, C.-C. Chen, P.A. van Aken, J. Maier, Y. Yu, Ge/C nanowires as high-capacity and long-life anode materials for Li-ion batteries, ACS Nano 8 (7) (2014) 7051–7059, http://dx.doi.org/10.1021/nn501945f.

[6] K. Ui, S. Kikuchi, Y. Kadoma, N. Kumagai, S. Ito, Electrochemical characteristics of Sn film prepared by pulse electrodeposition method as negative electrode for lithium secondary batteries, J. Power Sources 189 (1) (2009) 224–229, http://dx.doi.org/10.1016/j.jpowsour.2008.09.081.

[7] H. Tavassol, M.W. Cason, R.G. Nuzzo, A.A. Gewirth, Influence of oxides on the stress evolution and reversibility during SnO_x conversion and Li-Sn alloying reactions, Adv. Energy Mater. 5 (1) (2014) http://dx.doi.org/10.1002/aenm.201400317.

[8] A. Mukhopadhyay, R. Kali, S. Badjate, A. Tokranov, B.W. Sheldon, Plastic deformation associated with phase transformations during lithiation/delithiation of Sn, Scr. Mater. 92 (2014) 47–50, http://dx.doi.org/10.1016/j.scriptamat.2014.08.011.

[9] Y. Lu, Y. Ni, Effects of particle shape and concurrent plasticity on stress generation during lithiation in particulate Li-ion battery electrodes, Mech. Mater. 91 (2015) 372–381, http://dx.doi.org/10.1016/j.mechmat.2015.03.010.

[10] T. Danner, G. Zhu, A.F. Hofmann, A. Latz, Modeling of nano-structured cathodes for improved lithium-sulfur batteries, Electrochim. Acta 184 (2015) 124–133, http://dx.doi.org/10.1016/j.electacta.2015.09.143.

[11] J. Hou, S. Qu, M. Yang, J. Zhang, Materials and electrode engineering of high capacity anodes in lithium ion batteries, J. Power Sources 450 (2020) 227697, http://dx.doi.org/10.1016/j.jpowsour.2019.227697.

[12] X. Wang, F. Fan, J. Wang, H. Wang, S. Tao, A. Yang, Y. Liu, H. Beng Chew, S.X. Mao, T. Zhu, S. Xia, High damage tolerance of electrochemically lithiated silicon, Nat. Commun. 6 (1) (2015) 8417, http://dx.doi.org/10.1038/ncomms9417.

[13] X. Zhou, T. Li, Y. Cui, Y. Fu, Y. Liu, L. Zhu, In situ focused ion beam scanning electron microscope study of microstructural evolution of single tin particle anode for Li-ion batteries, ACS Appl. Mater. Interfaces 11 (2) (2019) 1733–1738, http://dx.doi.org/10.1021/acsami.8b13981.

[14] L. Beaulieu, S. Beattie, T. Hatchard, J. Dahn, The electrochemical reaction of lithium with tin studied by in situ AFM, J. Electrochem. Soc. 150 (4) (2003) A419, http://dx.doi.org/10.1149/1.1556595.

[15] K.J. Rhodes, R. Meisner, M. Kirkham, N. Dudney, C. Daniel, In situ XRD of thin film tin electrodes for lithium ion batteries, J. Electrochem. Soc. 159 (3) (2012) A294, http://dx.doi.org/10.1149/2.077203jes.

[16] J. Wang, D.X. Liu, M. Canova, R.G. Downing, L.R. Cao, A.C. Co, Profiling lithium distribution in Sn anode for lithium-ion batteries with neutrons, J. Radioanal. Nucl. Chem. 301 (2014) 277–284, http://dx.doi.org/10.1007/s10967-014-3102-5.

[17] C.-H. Chen, E. Chason, P.R. Guduru, Numerical solution of moving phase boundary and diffusion-induced stress of Sn anode in the lithium-ion battery, J. Electrochem. Soc. 164 (11) (2017) E3661, http://dx.doi.org/10.1149/2.0661711jes.

[18] D.X. Liu, J. Wang, K. Pan, J. Qiu, M. Canova, L.R. Cao, A.C. Co, In situ quantification and visualization of lithium transport with neutrons, Angew. Chem. 126 (36) (2014) 9652–9656, http://dx.doi.org/10.1002/ange.201404197.

[19] G. Derrien, J. Hassoun, S. Panero, B. Scrosati, Nanostructured Sn-C composite as an advanced anode material in high-performance lithium-ion batteries, Adv. Mater. 19 (17) (2007) 2336–2340, http://dx.doi.org/10.1002/adma.200700748.

[20] G. Wang, M. Aubin, A. Mehta, H. Tian, J. Chang, A. Kushima, Y. Sohn, Y. Yang, Stabilization of Sn anode through structural reconstruction of a Cu-Sn intermetallic coating layer, Adv. Mater. 32 (42) (2020) 2003684, http://dx.doi.org/10.1002/adma.202003684.

[21] Y. Xu, Q. Liu, Y. Zhu, Y. Liu, A. Langrock, M.R. Zachariah, C. Wang, Uniform nano-Sn/C composite anodes for lithium ion batteries, Nano Lett. 13 (2) (2013) 470–474, http://dx.doi.org/10.1021/nl303823k.

[22] L. Xue, Z. Fu, Y. Yao, T. Huang, A. Yu, Three-dimensional porous Sn-Cu alloy anode for lithium-ion batteries, Electrochim. Acta 55 (24) (2010) 7310–7314, http://dx.doi.org/10.1016/j.electacta.2010.07.015.

[23] X.-L. Wang, W.-Q. Han, J. Chen, J. Graetz, Single-crystal intermetallic M-Sn (M=Fe, Cu, Co, Ni) nanospheres as negative electrodes for lithium-ion batteries, ACS Appl. Mater. Interfaces 2 (5) (2010) 1548–1551, http://dx.doi.org/10.1021/am100218v.

[24] A. Kitada, N. Fukuda, T. Ichii, H. Sugimura, K. Murase, Lithiation behavior of single-phase Cu-Sn intermetallics and effects on their negative-electrode properties, Electrochim. Acta 98 (2013) 239–243, http://dx.doi.org/10.1016/j.electacta.2013.03.035.

[25] L. Li, X. Liu, S. Wang, W. Zhao, Influence of surface structure on the capacity and irreversible capacity loss of Sn-based anodes for lithium ion batteries, ACS Sustain. Chem. Eng. 2 (7) (2014) 1857–1863, http://dx.doi.org/10.1021/sc500202m.

[26] F. Zhang, S. Liu, J. Wang, Y. Du, W. Zhang, H. Seifert, Thermal stability of ternary compounds in the Cu-Li-Sn system and phase transition of the Cu_6Sn_5 electrode: First-principles calculations and experiment, J. Alloys Compd. 783 (2019) 44–54, http://dx.doi.org/10.1016/j.jallcom.2018.12.292.

[27] X.-L. Wang, M. Feygenson, H. Chen, C.-H. Lin, W. Ku, J. Bai, M.C. Aronson, T.A. Tyson, W.-Q. Han, Nanospheres of a new intermetallic $FeSn_5$ phase: synthesis, magnetic properties and anode performance in Li-ion batteries, J. Am. Chem. Soc. 133 (29) (2011) 11213–11219, http://dx.doi.org/10.1021/ja202243j.

[28] B. Philippe, A. Mahmoud, J.-B. Ledeuil, M.T. Sougrati, K. Edström, R. Dedryvère, D. Gonbeau, P.-E. Lippens, $MnSn_2$ electrodes for Li-ion batteries: mechanisms at the nano scale and electrode/electrolyte interface, Electrochim. Acta 123 (2014) 72–83, http://dx.doi.org/10.1016/j.electacta.2014.01.010.

[29] M. He, M. Walter, K.V. Kravchyk, R. Erni, R. Widmer, M.V. Kovalenko, Monodisperse SnSb nanocrystals for Li-ion and Na-ion battery anodes: synergy and dissonance between Sn and Sb, Nanoscale 7 (2) (2015) 455–459, http: //dx.doi.org/10.1039/C4NR05604C.

[30] L. Simonin, U. Lafont, E. Kelder, SnSb micron-sized particles for Li-ion batteries, J. Power Sources 180 (2) (2008) 859–863, http://dx.doi.org/10.1016/j.jpowsour.2008.03.014.

[31] J. Yin, M. Wada, S. Tanase, T. Sakai, Electrode properties and lithiation/delithiation reactions of Ag-Sb-Sn nanocomposite anodes in Li-ion batteries, J. Electrochem. Soc. 151 (6) (2004) A867, http://dx.doi.org/10.1149/1.1710515.

[32] J. Hassoun, S. Panero, G. Mulas, B. Scrosati, An electrochemical investigation of a Sn-Co-C ternary alloy as a negative electrode in Li-ion batteries, J. Power Sources 171 (2) (2007) 928–931, http://dx.doi.org/10.1016/j.jpowsour.2007.06.067.

[33] Q. Fan, P.J. Chupas, M.S. Whittingham, Characterization of amorphous and crystalline tin-cobalt anodes, Electrochem. Solid-State Lett. 10 (12) (2007) A274, http://dx.doi.org/10.1149/1.2789418.

[34] X.-L. Wang, H. Chen, J. Bai, W.-Q. Han, $CoSn_5$ phase: crystal structure resolving and stable high capacity as anodes for Li ion batteries, J. Phys. Chem. Lett. 3 (11) (2012) 1488–1492, http://dx.doi.org/10.1021/jz300461h.

[35] K. Zhuo, M.-G. Jeong, C.-H. Chung, Highly porous dendritic Ni-Sn anodes for lithium-ion batteries, J. Power Sources 244 (2013) 601–605, http://dx.doi.org/10.1016/j.jpowsour.2013.01.055.

[36] B. Polat, A. Abouimrane, N. Sezgin, O. Keles, K. Amine, Use of multilayered Ni-Sn and Ni-Sn-C thin film anodes for lithium-ion batteries, Electrochim. Acta 135 (2014) 585–593, http://dx.doi.org/10.1016/j.electacta.2014.05.024.

[37] W. Pu, X. He, J. Ren, C. Wan, C. Jiang, Electrodeposition of Sn-Cu alloy anodes for lithium batteries, Electrochim. Acta 50 (20) (2005) 4140–4145, http://dx.doi.org/10.1016/j.electacta.2005.01.041.

[38] D.H. Nam, R.H. Kim, D.W. Han, H.S. Kwon, Electrochemical performances of Sn anode electrodeposited on porous Cu foam for Li-ion batteries, Electrochim. Acta 66 (2012) 126–132, http://dx.doi.org/10.1016/j.electacta.2012.01.084.

[39] I. Steinbach, F. Pezzolla, B. Nestler, M. Seeßelberg, R. Prieler, G.J. Schmitz, J.L. Rezende, A phase field concept for multiphase systems, Physica D 94 (3) (1996) 135–147, http://dx.doi.org/10.1016/0167-2789(95)00298-7.

[40] B. Nestler, A multiphase-field model: sharp interface asymptotics and numerical simulations of moving phase boundaries and multijunctions, J. Cryst. Growth 204 (1–2) (1999) 224–228, http://dx.doi.org/10.1016/S0022-0248(99)00154-2.

[41] L.-Q. Chen, Phase-field models for microstructure evolution, Annu. Rev. Mater. Sci. 32 (1) (2002) 113–140, http://dx.doi.org/10.1146/annurev.matsci.32.112001.132041.

[42] B. Han, A. Van der Ven, D. Morgan, G. Ceder, Electrochemical modeling of intercalation processes with phase field models, Electrochim. Acta 49 (26) (2004) 4691–4699, http://dx.doi.org/10.1016/j.electacta.2004.05.024.

[43] C.V. Di Leo, E. Rejovitzky, L. Anand, A Cahn–Hilliard-type phase-field theory for species diffusion coupled with large elastic deformations: application to phase-separating Li-ion electrode materials, J. Mech. Phys. Solids 70 (2014) 1–29, http://dx.doi.org/10.1016/j.jmps.2014.05.001.

[44] L. Chen, F. Fan, L. Hong, J. Chen, Y.Z. Ji, S. Zhang, T. Zhu, L. Chen, A phase-field model coupled with large elasto-plastic deformation: application to lithiated silicon electrodes, J. Electrochem. Soc. 161 (11) (2014) F3164, http://dx.doi.org/10.1149/2.0171411jes.

[45] N.J. De Klerk, A. Vasileiadis, R.B. Smith, M.Z. Bazant, M. Wagemaker, Explaining key properties of lithiation in TiO_2-anatase Li-ion battery electrodes using phase-field modeling, Phys. Rev. Mater. 1 (2) (2017) 025404, http://dx.doi.org/10.1103/PhysRevMaterials.1.025404.

[46] S. Hu, Y. Li, K.M. Rosso, M.L. Sushko, Mesoscale phase-field modeling of charge transport in nanocomposite electrodes for lithium-ion batteries, J. Phys. Chem. C 117 (1) (2013) 28–40, http://dx.doi.org/10.1021/jp3068014.

[47] L. Chang, Y. Lu, L. He, Y. Ni, Phase field model for two-phase lithiation in an arbitrarily shaped elastoplastic electrode particle under galvanostatic and potentiostatic operations, Int. J. Solids Struct. 143 (2018) 73–83, http://dx.doi.org/10.1016/j.ijsolstr.2018.02.033.

[48] Y. Lu, L. Chang, H. Yao, L. He, Y. Ni, Transition from deceleration to acceleration of lithiation front movement in hollow phase transformation electrodes, J. Electrochem. Soc. 164 (13) (2017) A3371, http://dx.doi.org/10.1149/2.0781713jes.

[49] S. Daubner, M. Weichel, D. Schneider, B. Nestler, Modeling intercalation in cathode materials with phase-field methods: Assumptions and implications using the example of $LiFePO_4$, Electrochim. Acta 421 (2022) 140516, http://dx.doi.org/10.1016/j.electacta.2022.140516.

[50] S. Daubner, M. Dillenz, L. Pfeiffer, C. Gauckler, M. Rosin, N. Burgard, J. Martin, P. Axmann, M. Sotoudeh, A. Gross, D. Schneider, B. Nestler, Combined study of phase transitions in the P2-type $Na_xNi_{1/3}Mn_{2/3}O_2$ cathode material: experimental, ab-initio and multiphase-field results, 2023, http://dx.doi.org/10.21203/rs.3.rs-3125461/v1.

[51] Q. Huang, S. Daubner, S. Zhang, D. Schneider, B. Nestler, H. Mao, S. Liu, Y. Du, Phase-field simulation for voltage profile of Li_xSn nanoparticle during lithiation/delithiation, Comput. Mater. Sci. 220 (2023) 112047, http://dx.doi.org/10.1016/j.commatsci.2023.112047.

[52] S. Fürtauer, D. Li, D. Henriques, A. Beutl, H. Giel, D. Cupid, T. Markus, H. Flandorfer, Phase diagram, thermodynamic investigations, and modelling of systems relevant to lithium-ion batteries, Int. J. Mater. Res. 108 (11) (2017) 887–903, http://dx.doi.org/10.3139/146.111561.

[53] W. Zhang, D.M. Cupid, P. Gotcu, K. Chang, D. Li, Y. Du, H.J. Seifert, High-throughput description of infinite composition-structure-property-performance relationships of lithium-manganese oxide spinel cathodes, Chem. Mater. 30 (7) (2018) 2287–2298, http://dx.doi.org/10.1021/acs.chemmater.7b05068.

[54] N. Dubouis, C. Park, M. Deschamps, S. Abdelghani-Idrissi, M. Kanduč, A. Colin, M. Salanne, J. Dzubiella, A. Grimaud, B. Rotenberg, Chasing aqueous biphasic systems from simple salts by exploring the LiTFSI/LiCl/H_2O phase diagram, ACS Central Science 5 (4) (2019) 640–643, http://dx.doi.org/10.1021/acscentsci.8b00955, PMID: 31041383.

[55] J.M. Weller, M.M. Li, E. Polikarpov, K.S. Han, N. Kidner, A. Patel, M. Nguyen, M. Stout, M. Gossett, K. Jung, D.M. Reed, V.L. Sprenkle, G. Li, Unlocking the NaCl-$AlCl_3$ phase diagram for low-cost, long-duration Na-Al batteries, Energy Storage Mater. 56 (2023) 108–120, http://dx.doi.org/10.1016/j.ensm.2023.01.009.

[56] R. Berthelot, D. Carlier, C. Delmas, Electrochemical investigation of the P2-Na_xCoO_2 phase diagram, Nat. Mater. 10 (1) (2011) 74–80, http://dx.doi.org/10.1038/nmat2920.

[57] H.-C. Yu, H.-Y. Chen, K. Thornton, Extended smoothed boundary method for solving partial differential equations with general boundary conditions on complex boundaries, Modelling Simul. Mater. Sci. Eng. 20 (7) (2012) 075008, http://dx.doi.org/10.1088/0965-0393/20/7/075008.

[58] A. Choudhury, B. Nestler, Grand-potential formulation for multicomponent phase transformations combined with thin-interface asymptotics of the double-obstacle potential, Phys. Rev. E 85 (2) (2012) 021602, http://dx.doi.org/10.1103/PhysRevE.85.021602.

[59] I. Steinbach, Phase-field models in materials science, Model. Simul. Mater. Sci. Eng. 17 (7) (2009) 073001, http://dx.doi.org/10.1088/0965-0393/17/7/073001.

[60] Y.U. Wang, Y.M. Jin, A.G. Khachaturyan, Phase field microelasticity theory and modeling of elastically and structurally inhomogeneous solid, J. Appl. Phys. 92 (3) (2002) 1351–1360, http://dx.doi.org/10.1063/1.1492859.

[61] D. Schneider, S. Schmid, M. Selzer, T. Böhlke, B. Nestler, Small strain elasto-plastic multiphase-field model, Comput. Mech. 55 (2015) 27–35, http://dx.doi.org/10.1007/s00466-014-1080-7.

[62] W. Schmickler, E. Santos, Interfacial Electrochemistry, Springer Science & Business Media, 2010, doi:https://link.springer.com/book/10.1007/978-3-642-04937-8.

[63] I. Steinbach, F. Pezzolla, A generalized field method for multiphase transformations using interface fields, Physica D 134 (4) (1999) 385–393, http://dx.doi.org/10.1016/S0167-2789(99)00129-3.

[64] P.K. Amos, E. Schoof, D. Schneider, B. Nestler, Chemo-elastic phase-field simulation of the cooperative growth of mutually-accommodating Widmanstätten plates, J. Alloys Compd. 767 (2018) 1141–1154, http://dx.doi.org/10.1016/j.jallcom.2018.07.138.

[65] E. Schoof, D. Schneider, N. Streichhan, T. Mittnacht, M. Selzer, B. Nestler, Multiphase-field modeling of martensitic phase transformation in a dual-phase microstructure, Int. J. Solids Struct. 134 (2018) 181–194, http://dx.doi.org/10.1016/j.ijsolstr.2017.10.032.

[66] L. Chang, Y. Lu, L. He, Y. Ni, Phase field model for two-phase lithiation in an arbitrarily shaped elastoplastic electrode particle under galvanostatic and potentiostatic operations, Int. J. Solids Struct. 143 (2018) 73–83, http://dx.doi.org/10.1016/j.ijsolstr.2018.02.033.

[67] Q. Li, P. Wang, Q. Feng, M. Mao, J. Liu, S.X. Mao, H. Wang, In situ TEM on the reversibility of nanosized sn anodes during the electrochemical reaction, Chem. Mater. 26 (14) (2014) 4102–4108, http://dx.doi.org/10.1021/cm5009448.

[68] L. Chen, H.W. Zhang, L.Y. Liang, Z. Liu, Y. Qi, P. Lu, J. Chen, L.-Q. Chen, Modulation of dendritic patterns during electrodeposition: A nonlinear phase-field model, J. Power Sources 300 (2015) 376–385.

[69] L. Chang, Y. Lu, D. Lei, H. Liu, L. He, Y. Ni, Y. Li, High rate capability composite particles with root-inspired hierarchical channel structure, J. Power Sources 494 (2021) 229777.

[70] I.A. Courtney, J. Tse, O. Mao, J. Hafner, J.R. Dahn, Ab initio calculation of the lithium-tin voltage profile, Phys. Rev. B 58 (23) (1998) 15583, http://dx.doi.org/10.1103/PhysRevB.58.15583.

[71] J. Gao, S.-Q. Shi, H. Li, Brief overview of electrochemical potential in lithium ion batteries, Chin. Phys. B 25 (1) (2015) 018210, http://dx.doi.org/10.1088/1674-1056/25/1/018210.

[72] F. Zhang, J. Wang, S. Liu, Y. Du, Effects of the volume changes and elastic-strain energies on the phase transition in the Li-Sn battery, J. Power Sources 330 (2016) 111–119, http://dx.doi.org/10.1016/j.jpowsour.2016.08.136.

[73] A.T. Dinsdale, SGTE data for pure elements, CALPHAD 15 (4) (1991) 317–425, http://dx.doi.org/10.1016/0364-5916(91)90030-N.

[74] Q. Huang, Microstructure intelligent design (MInDes), 2023, doi:https://github.com/Microstructure-Intelligent-Design/MInDes.

[75] R. Chandra, Parallel Programming in OpenMP, Morgan Kaufmann, 2001, doi:https://shop.elsevier.com/books/parallel-programming-in-openmp/chandra/978-1-55860-671-5.

[76] K. Eom, J. Jung, J.T. Lee, V. Lair, T. Joshi, S.W. Lee, Z. Lin, T.F. Fuller, Improved stability of nano-Sn electrode with high-quality nano-SEI formation for lithium ion battery, Nano Energy 12 (2015) 314–321.

[77] H. Ying, W.-Q. Han, Metallic Sn-based anode materials: application in high-performance lithium-ion and sodium-ion batteries, Adv. Sci. 4 (11) (2017) 1700298, http://dx.doi.org/10.1002/advs.201700298.

[78] C.-H. Chen, E. Chason, P.R. Guduru, Numerical solution of moving phase boundary and diffusion-induced stress of Sn anode in the lithium-ion battery, J. Electrochem. Soc. 164 (11) (2017) E3661, http://dx.doi.org/10.1149/2.0661711jes.

[79] C.S. Hong, N. Qaiser, H.G. Nam, S.M. Han, Effect of Li concentration-dependent material properties on diffusion induced stresses of a Sn anode, Phys. Chem. Chem. Phys. 21 (2019) 9581–9589, http://dx.doi.org/10.1039/C9CP00559E.

[80] K. Hirai, T. Ichitsubo, T. Uda, A. Miyazaki, S. Yagi, E. Matsubara, Effects of volume strain due to Li-Sn compound formation on electrode potential in lithium-ion batteries, Acta Mater. 56 (7) (2008) 1539–1545, http://dx.doi.org/10.1016/j.actamat.2007.12.002.